# Leading-edge receptivity to free-stream disturbance waves for hypersonic flow over a parabola

By XIAOLIN ZHONG

Mechanical and Aerospace Engineering Department, University of California, Los Angeles,
CA 90095, USA

The receptivity of hypersonic boundary layers to free-stream disturbances, which is the process of environmental disturbances initially entering the boundary layers and generating disturbance waves, is altered considerably by the presence of bow shocks in hypersonic flow fields. This paper presents a numerical simulation study of the generation of boundary layer disturbance waves due to free-stream waves, for a two-dimensional Mach 15 viscous flow over a parabola. Both steady and unsteady flow solutions of the receptivity problem are obtained by computing the full Navier–Stokes equations using a high-order-accurate shock-fitting finite difference scheme. The effects of bow-shock/free-stream-sound interactions on the receptivity process are accurately taken into account by treating the shock as a discontinuity surface, governed by the Rankine-Hugoniot relations. The results show that the disturbance waves generated and developed in the hypersonic boundary layer contain both first-, second-, and third-mode waves. A parametric study is carried out on the receptivity characteristics for different free-stream waves, frequencies, nose bluntness characterized by Strouhal numbers, Reynolds numbers, Mach numbers, and wall cooling. In this paper, the hypersonic boundary-layer receptivity is characterized by a receptivity parameter defined as the ratio of the maximum induced wave amplitude in the first-mode-dominated region to the amplitude of the free-stream forcing wave. It is found that the receptivity parameter decreases when the forcing frequency or nose bluntness increase. The results also show that the generation of boundary layer waves is mainly due to the interaction of the boundary layer with the acoustic wave field behind the bow shock, rather than interactions with the entropy and vorticity wave fields.

## 1. Introduction

The prediction of laminar–turbulent transition in hypersonic boundary layers is a critical part of the aerodynamic design and control of hypersonic vehicles. The transition process is a result of the nonlinear response of laminar boundary layers to forcing disturbances (Reshotko 1991), which can originate from many different sources including free-stream disturbances, surface roughness and vibrations. In an environment with weak initial disturbances, the path to transition consists of three stages: (i) receptivity, (ii) linear eigenmode growth or transient growth, and (iii) nonlinear breakdown to turbulence. The first stage is the receptivity process (Morkovin 1969), which converts the environmental disturbances into initial disturbance waves in the boundary layers. The second stage is the subsequent linear development and

growth of boundary-layer instability waves. Relevant instability waves for hypersonic boundary layers include the first-mode and higher-mode instabilities (Mack 1984), the Görtler instability over concave surfaces, the attachment line instability at leading edges, and the cross-flow instability in three-dimensional boundary layers. The third stage is the breakdown of linear instability waves, and the transition to turbulence after the linear instability waves reach certain magnitudes.

The stability and transition of supersonic and hypersonic boundary layers has been reviewed by Mack (1984), Reshotko (1991), and many others. Most of our knowledge of hypersonic boundary layer stability is obtained by the linear stability theory (LST) (Mack 1984). Lees & Lin (1946) showed that the existence of a generalized inflection point is a necessary condition for inviscid instability in a compressible boundary layer. Mack (1984) found that there are higher acoustic instability modes in addition to the first-mode instability waves in supersonic and hypersonic boundary layers. Among them, the second mode becomes the dominant instability for hypersonic boundary layers at Mach numbers larger than about 4. The existence and dominance of the second mode has been validated by experimental studies (Stetson & Kimmel 1992). Experimental measurements on hypersonic boundary layer stability on sharp cones have been performed by Kendall (1975) and others. The results indicated that the first- and second-mode instabilities are simultaneously present in hypersonic boundary layers.

Practical hypersonic vehicles have blunt noses in order to reduce thermal loads. It has been generally recognized that the bow shock in front of a blunt nose has a strong effect on the stability and transition of the boundary layer behind it (Reshotko 1991). Reshotko & Khan (1980) showed that the swallowing of the entropy layer by a boundary layer has a strong effect on the boundary-layer stability. These effects on hypersonic boundary layer transition have been studied in experiments (Potter & Whitfield 1962; Stetson *et al.* 1984). Experimental results show that an increase of nose bluntness delays transition, but the trend is reversed when the nose bluntness exceeds a certain limit. Stetson *et al.* (1984) also found evidence of inviscid entropy instability in the region outside the boundary layers for blunt cones in a Mach 8 free stream. The stability characteristics of hypersonic boundary layers over a blunt cone corresponding to Stetson's experiments have been studied using the linear stability analysis (Malik, Spall & Chang 1990; Herbert & Esfahanian 1993; Kufner, Dallmann & Stilla 1993). Though some observations on the effects of bluntness and the entropy layer are consistent with linear stability analysis, the second-mode instability and the general amplification characteristics in the blunt cone flows do not agree with the experiments. The discrepancy may be due to the fact that it is difficult to obtain highly accurate steady base flow solutions of hypersonic flow over blunt cones, for the stability analysis. The effects of bow shocks and non-parallel boundary layers are neglected in a normal-mode stability analysis. In addition, the initial receptivity process, which becomes very complex due to hypersonic bow shock interaction, is not considered in the linear stability analysis.

This paper is concerned with the receptivity process of hypersonic boundary layer flows over blunt leading edges. The receptivity mechanism provides important initial conditions of amplitude, frequency, and phase of instability waves in the boundary layers. Theoretical results on incompressible boundary layer receptivity are mainly obtained based on the asymptotic theory (Goldstein 1983). The asymptotic analysis explains how the long-wavelength free-stream acoustic disturbances enter the boundary layer and generate short-wavelength Tollmien–Schlichting (T–S) waves in incompressible boundary layers. Direct numerical simulations, which solve the full
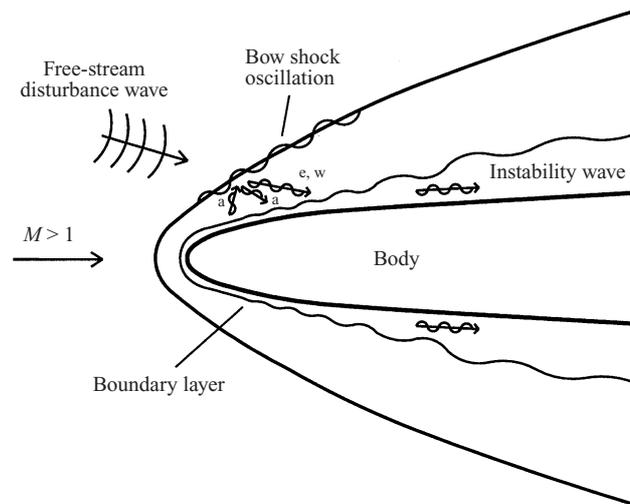
FIGURE 1. A schematic of the wave field of the interaction between a bow shock and free-stream disturbances in the leading-edge receptivity process. a: acoustic wave, e: entropy wave, w: vorticity wave.

Navier–Stokes equations as an initial-boundary problem, have become an important tool in receptivity and transition studies in recent years. Direct numerical simulations of the receptivity of incompressible or subsonic boundary layers have been performed by Murdock (1981), Buter & Reed (1994), Casalis & Cantaloube (1994), and Collis & Lele (1996). For hypersonic boundary-layer flows over blunt bodies, the receptivity phenomena are much more complex and are currently not well understood (Reshotko 1991). Only a few studies have been reported on the receptivity of hypersonic boundary layers. Choudhari & Streett (1993) extended the asymptotic theory to the prediction of receptivity in a Mach 4.5 boundary layer with a zero pressure gradient. The effects of shock interaction were not considered.

Figure 1 shows a schematic of wave interactions in the leading edge region of a hypersonic flow in the presence of free-stream disturbances. The receptivity phenomena are altered considerably by the bow shock in front of the body. The interaction of free-stream waves with the shock affects the receptivity process of the boundary layer behind the shock. Kovasznay (1953) showed that weak disturbance waves in compressible flow can be decomposed into three independent modes: acoustic, entropy, and vorticity modes. The acoustic wave is propagated with the speed of sound relative to the moving fluid, while the entropy and vorticity waves convect with the moving fluid velocity. Before entering the boundary layer, free-stream disturbances first pass through and interact with the bow shock. Irrespective of the nature of a free-stream disturbance wave, its interaction with the bow shock always generates all three types of disturbance waves (McKenzie & Westphal 1968) after passing through the shock. These waves are propagated downstream and interact with the boundary layer on the body. At the same time, the perturbed boundary layer also generates reflected acoustic waves propagating upstream. When they return to impinge on the shock from behind, the reflected acoustic waves generate additional disturbances of all three kinds which also propagate downstream. Such back and forth reflections and interactions create a complex wave field behind the bow shock. The combined effects of these interactions determine the receptivity process of the hypersonic boundary layer behind the shock.

Owing to the complexity of transient hypersonic flow fields involving a receptivity process, an effective approach to studying hypersonic boundary layer receptivity is the direct numerical simulation of the full time-dependent three-dimensional Navier–Stokes equations for the temporally or spatially evolving instability waves. Such a simulation requires that all relevant flow time and length scales are resolved and so highly accurate high-order numerical methods are required. One of the difficulties in hypersonic flow simulations is that, owing to numerical instability, high-order linear schemes can only be used for the spatial discretization of the equations in flow fields without shock waves. In Zhong (1998), we presented and validated a new high-order (fifth and sixth order) upwind finite difference shock-fitting method for the direct numerical simulation of hypersonic flows with a strong bow shock and with stiff source terms. There are three main aspects of this method for transient hypersonic flows: a new shock fitting formulation, new upwind high-order finite difference schemes, and recently derived third-order semi-implicit Runge–Kutta schemes (Zhong 1996). The method has been validated and applied to numerical studies of receptivity of two- and three-dimensional hypersonic flows over blunt bodies.

The purpose of this paper is to study the receptivity of hypersonic boundary-layer flows to weak free stream disturbances, which are planar acoustic, entropy, and vorticity waves with fixed frequencies. The body is a parabolic leading edge. The generation of boundary-layer waves is studied using numerically obtained solutions of the nonlinear Navier–Stokes equations. The bow-shock oscillations and the effects of bow-shock/free-stream-sound interaction on the receptivity process are accurately taken into account by treating the shock as a moving discontinuity surface governed by the Rankine–Hugoniot relations. A parametric study is carried out by numerical simulations of a number of computational cases with different free-stream forcing waves, frequencies, forcing wave amplitudes, nose bluntness, Mach numbers, Reynolds numbers, and wall cooling. In order to focus our attention on the leading-edge receptivity, we limit the current study to the two-dimensional disturbance waves in hypersonic boundary layers induced by two-dimensional free-stream disturbances. The receptivity of three-dimensional wave interactions is a subject of a separate study, and is not considered here. Since the receptivity of the fundamental frequency is linear with respect to weak forcing waves, any weak disturbances in the free stream can be decomposed into a linear combination of single-frequency Fourier modes. Numerical solutions of the full Navier–Stokes equations are compared with theoretical analysis, such as the local normal-mode linear stability analysis, for the purpose of analysing the numerical results. The numerical accuracy of the computational results is evaluated by a grid refinement study and by comparison with available experimental or theoretical results. Detailed results of the code validation and error assessment have been reported in Zhong (1998). They are not repeated in this paper.

## 2. Governing equations

The following gas models are used in the present study of the receptivity of hypersonic flow over a parabolic leading edge. The gas is assumed to be a thermally and calorically perfect gas governed by the continuum Navier–Stokes equations. The viscosity coefficients are calculated according to the Sutherland law with the assumption of zero bulk viscosity. The heat conductivity coefficients are determined by assuming a constant Prandtl number. The bow shock is assumed to be thin so that it is treated as a mathematically discontinuous surface satisfying the Rankine–Hugoniot relations. This flow model corresponds to ground-based 'cold' hypersonic

experiments where high Mach numbers are achieved in wind tunnels at relatively low stagnation temperatures. For such hypersonic flows, the real gas effects are not excited because of low gas temperatures. So far, most of the reported hypersonic experimental and theoretical studies on stability and transition are in such flow regimes. Examples are Kendall (1975), Stetson *et al.* (1984), and Stetson & Kimmel (1992) for experiments and Herbert & Esfahanian (1993) and Kufner *et al.* (1993) for theoretical works. The perfect gas assumption is necessary because the stability and transition of hypersonic boundary layers is mostly a hydrodynamic problem governed by the perfect gas flow equations. For 'hot' hypersonic flows, which are often termed 'hypervelocity' flows, high-temperature real gas effects are significant. Such effects include non-equilibrium thermal excitation and chemical dissociation. In addition, rarefied gas effects may become significant because many hypersonic vehicles operate in low Reynolds number and high Mach number conditions. The bow shock may not be very thin in rarefied gas flow. These real gas effects may introduce strong modifications to the stability and transition properties, but they can be studied separately. Therefore, like most other hypersonic boundary-layer stability and transition studies, perfect-gas flow equations are used in this paper in order to bring out the main hydrodynamic features of their receptivity. Real and rarefied gas effects are important but separate and are not considered in this paper.

The governing equations are the unsteady three-dimensional Navier–Stokes equations written in the following conservation-law form:

$$\frac{\partial \boldsymbol{U}^*}{\partial t^*} + \frac{\partial \boldsymbol{F}_j^*}{\partial x_j^*} + \frac{\partial \boldsymbol{F}_{vj}^*}{\partial x_j^*} = 0 \tag{1}$$

where the superscript $*$ represents dimensional variables, and $x_j^*$ and $t^*$ are independent variables of Cartesian coordinates and time respectively. The vector of the conservative flow variables is

$$\boldsymbol{U}^* = \{\rho^*, \rho^* u_1^*, \ \rho^* u_2^*, \ \rho^* u_3^*, \ e^*\}. \tag{2}$$

The equations of state are $p^* = \rho^* R^* T^*$ and $e^* = \rho^*(c_v^* T^* + \frac{1}{2} u_k^* u_k^*)$, where the gas constant $R^*$ and the specific heats $c_p^*$ and $c_v^*$ are assumed to be constants. The flux vectors in (1) are

$$\boldsymbol{F}_j^* = \left\{ \begin{array}{c} \rho^* u_j^* \\ \rho^* u_1^* u_j^* + p^* \delta_{1j} \\ \rho^* u_2^* u_j^* + p^* \delta_{2j} \\ \rho^* u_3^* u_j^* + p^* \delta_{3j} \\ (e^* + p^*) u_j^* \end{array} \right\}, \quad \boldsymbol{F}_{vj}^* = \left\{ \begin{array}{c} 0 \\ -\tau_{1j}^* \\ -\tau_{2j}^* \\ -\tau_{3j}^* \\ -\tau_{jk}^* u_k^* - q_j^* \end{array} \right\}, \tag{3}$$

where the viscous stress tensor and heat flux vector are

$$\tau_{ij}^* = \mu^* \left( \frac{\partial u_i^*}{\partial x_j^*} + \frac{\partial u_j^*}{\partial x_i^*} \right) - \frac{2}{3} \mu^* \frac{\partial u_k^*}{\partial x_k^*} \delta_{ij}, \quad q_j^* = -\kappa^* \frac{\partial T^*}{\partial x_j^*}. \tag{4}$$

where $\mu^*$ is the viscosity coefficient determined by Sutherland's law,

$$\mu^* = \mu_r^* \left( \frac{T^*}{T_r^*} \right)^{3/2} \frac{T_r^* + T_s^*}{T^* + T_s^*},$$

and $\kappa^*$ is the heat conductivity coefficient determined by assuming a constant Prandtl number defined by $Pr = \mu^* c_p^* / \kappa^*$.

In a leading-edge receptivity problem, both steady and unsteady flow solutions of the Navier–Stokes equations are computed by numerical simulations. For a steady flow simulation, flow variables for the supersonic free stream in front of the bow shock are constant, while for an unsteady flow they are time varying acoustic wave fields. The body surface is assumed to be a non-slip isothermal wall with a given temperature $T_w^*$. The bow shock is assumed to be an infinitely thin moving discontinuity surface, where flow variables across the shock are governed by the Rankine-Hugoniot conditions. These lead to jump conditions for flow variables behind the moving shock as functions of unsteady free stream flow variables at the shock and the local shock normal velocity $v_n^*$, i.e.

$$p_s^* = p_1^* \left[ 1 + \frac{2\gamma}{\gamma + 1}(M_{n1}^2 - 1) \right],$$  (5)

$$\rho_s^* = \rho_1^* \left[ \frac{(\gamma + 1)M_{n1}^2}{(\gamma - 1)M_{n1}^2 + 2} \right],$$  (6)

$$u_{ns}^* = v_n^* + \frac{\rho_1^*}{\rho_s^*}(u_{n1}^* - v_n^*),$$  (7)

$$\boldsymbol{u}_{ts}^* = \boldsymbol{u}_{t1}^* = \boldsymbol{u}_1^* - u_{n1}^*\boldsymbol{n},$$  (8)

$$\boldsymbol{u}_s^* = \boldsymbol{u}_{ts}^* + u_{ns}^*\boldsymbol{n} = \boldsymbol{u}_1^* + (u_{ns}^* - u_{n1}^*)\boldsymbol{n},$$  (9)

where $M_{n1} = (u_{n1}^* - v_n^*)/a_1^*$ is the normal component of the free-stream Mach number relative to the shock motion, $\boldsymbol{u}^*$ is the velocity vector, $\boldsymbol{u}_t^*$ is the tangential velocity vector, $u_n$ is the normal velocity component. In order to compute the flow variables behind the shock, the velocity of the shock front $v_n^*$ is needed. The shock normal velocity is determined by a characteristic compatibility equation immediately behind the shock. The details of the shock fitting formulas and numerical methods can be found in Zhong (1998).

Since flow variables behind the bow shock are not constant, they are non-dimensionalized using the steady-state free-stream conditions. Specifically, we non-dimensionalize the velocities with respect to the free-stream velocity $U_\infty^*$, length scales with respect to a reference length $d^*$, density with respect to $\rho_\infty^*$, pressure with respect to $p_\infty^*$, temperature with respect to $T_\infty^*$, time with respect to $d^*/U_\infty^*$, vorticity with respect to $U_\infty^*/d^*$, entropy with respect to $c_p^*$, wavenumber by $1/d^*$, etc. The dimensionless flow variables have no superscript asterisk.

## 3. Flow conditions

The receptivity of a two-dimensional boundary layer to free-stream waves for hypersonic flows past a parabolic leading edge at zero angle of attack is considered. The parabolic body surface is determined by

$$x^* = b^*y^{*2} - d^*,$$  (10)

where $b^*$ and $d^*$ are constants. The nose radius of curvature is $r^* = 1/(2b^*)$. Free stream disturbances are superimposed on a steady mean flow before it reaches the bow shock, to investigate the process of free stream waves entering the boundary layer and inducing boundary-layer waves. The free-stream disturbances are assumed to be weak monochromatic planar waves with wave fronts normal to the centreline of the body. The wave fields are represented by perturbations of instantaneous flow

variables with respect to the local steady base flow variables at the same location. For example, instantaneous velocity perturbation $u'$ located at $(x, y)$, at time $t$, is defined as:

$$u'(x, y, t) = u(x, y, t) - U(x, y), \qquad (11)$$

where $u(x, y, t)$ is the instantaneous velocity component obtained by an unsteady numerical simulation of the nonlinear Navier–Stokes equations, and $U(x, y)$ is the steady mean flow velocity obtained by a separate steady flow simulation.

There are four kinds of weak perturbation waves in a uniform flow in the free stream: fast acoustic waves, slow acoustic waves, entropy waves, and vorticity waves. For weak disturbance waves in the free stream before reaching the bow shock, the perturbation of an arbitrary flow variable can be written in the following form:

$$q_\infty(x, y, t)' = |q'_\infty| e^{ik_\infty(x - c_\infty t)}, \qquad (12)$$

where $q_\infty(x, y, t)$ represents the perturbation of any flow variable, $|q'_\infty|$ is the wave amplitude constant, $k_\infty$ is the wavenumber, and $c_\infty$ is the wave speed in the free stream before reaching the shock. For the four kinds of linear waves, perturbation amplitudes of non-dimensional flow variables satisfy the following dispersion relations:

fast acoustic waves ($c^*_\infty = u^*_\infty + a^*_\infty$)

$$|\rho'|_\infty = |p'|_\infty / \gamma = |u'|_\infty M_\infty = \epsilon M_\infty, |s'|_\infty = |v'|_\infty = 0;$$

slow acoustic waves ($c^*_\infty = u^*_\infty - a^*_\infty$)

$$|\rho'|_\infty = |p'|_\infty / \gamma = -|u'|_\infty M_\infty = \epsilon M_\infty, |s'|_\infty = |v'|_\infty = 0;$$

entropy waves ($c^*_\infty = u^*_\infty$)

$$|\rho'|_\infty = -|s'|_\infty = \epsilon M_\infty, |u'|_\infty = |v'|_\infty = |p'|_\infty = 0;$$

vorticity waves ($c^*_\infty = u^*_\infty$)

$$|v'|_\infty M_\infty = \epsilon M_\infty, |u'|_\infty = |p'|_\infty = |s'|_\infty = 0;$$

where $\epsilon$ is a small number, and $\epsilon M_\infty$ represents the relative amplitude of a free-stream wave. The free-stream wavenumber $k_\infty$ is related to the circular frequency $\omega$ by $\omega = k_\infty c_\infty$.

The flow is characterized by a free-stream Mach number $M_\infty = u^*_\infty / a^*_\infty$, and a Reynolds number $Re_\infty = \rho^*_\infty U^*_\infty d^* / \mu^*_\infty$. The forcing frequency of the free-stream acoustic wave is represented by a dimensionless frequency $F$ defined with respect to a viscous flow scale by

$$F = 10^6 \frac{\omega^* v^*}{U^{*2}_\infty} = 10^6 \omega / Re_\infty. \qquad (13)$$

We can also define a Strouhal number $S$ in terms of the nose radius $r^*$ by

$$S = \frac{\omega^* r^*}{U^*_\infty}. \qquad (14)$$

The Strouhal number represents the relative nose bluntness in the receptivity problem. The wall temperature is characterized by its ratio to the free-stream stagnation temperature, i.e.

$$\frac{T_w}{T_0} = \frac{T^*_w}{T^*_\infty \left(1 + \dfrac{\gamma - 1}{2} M^2_\infty\right)},$$
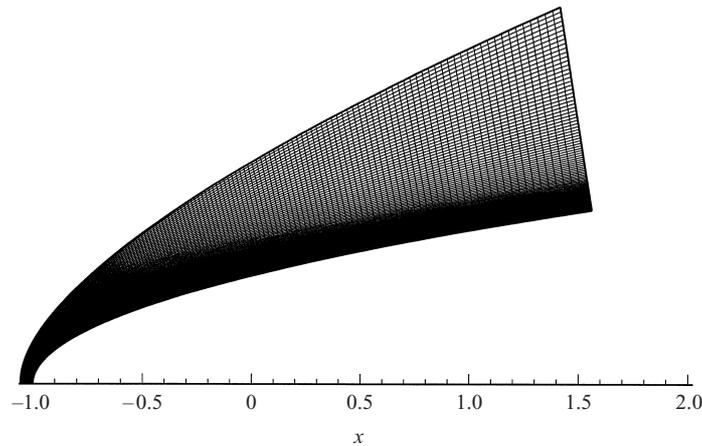
FIGURE 2. Computational grid for steady base flow solutions where the bow shock shape is
obtained as the numerical solution for the upper grid line boundary.

where $T_w^*$ and $T_\infty^*$ are the wall temperature and the free-stream temperature respectively.

The receptivity problems are studied numerically by solving the unsteady Navier–Stokes equations using a fifth-order shock-fitting scheme described in Zhong (1998). A numerical simulation is carried out in three steps. First, a steady flow field is computed by advancing the flow solutions to convergence with no disturbances imposed in the free stream. Second, unsteady viscous flows are computed by imposing a continuous planar acoustic single-frequency wave on the steady flow variables on the free-stream side of the bow shock. The unsteady simulation is made nonlinear by computing the transient flow solutions of the Navier–Stokes equations without any linearization in the equations and in the shock jump conditions. The wave interactions with the shock and the development of disturbance waves in the boundary layer are simultaneously resolved by the simulation. The unsteady calculations are carried out for about 20 to 40 temporal periods until the solutions reach a periodic state in time. Third, the unsteady computations are carried out for one additional period in time to record the perturbations with respect to the steady flow field obtained previously. A Fourier transform is performed on the perturbation variables to obtain the Fourier amplitudes and phase angles of the perturbations of the unsteady flow variables throughout the flow field.

Seven groups of computational cases are considered to study the effects of various flow parameters on the hypersonic receptivity process. The non-dimensional flow parameters are chosen for a typical Mach number and Reynolds number range for hypersonic flow over a leading edge. The first group involves free-stream planar acoustic waves, and is analysed in detail in §5. A parametric study is then carried out in §6 by considering six additional groups of computational cases to study the effects of different free-stream forcing waves, frequencies, nose bluntness, Reynolds numbers, Mach numbers, and wall cooling. The flow conditions of all seven groups (case A to case G) are tabulated in Appendix A.

Body-fitted grids are used in the computations, where the oscillating bow shock is treated as an outer computational boundary. Figure 2 shows a $160 \times 120$ computational grid for a Mach 15 steady base flow solution, where the upper grid line is the bow shock. The shape of the bow shock, which is not known in advance, is obtained as
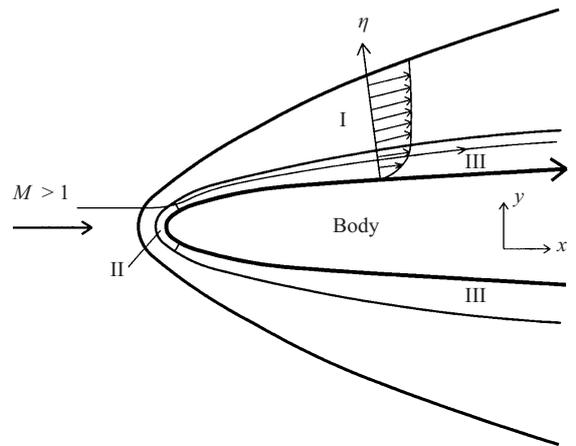
FIGURE 3. Classification of flow field regions for a viscous hypersonic flow over a blunt leading edge: I, inviscid rotational flow field; II, stagnation point region; III, boundary layer downstream.

a part of the base flow solution. A $320 \times 240$ grid is also used to repeat the steady and unsteady calculations to evaluate the numerical accuracy of the Navier-Stokes solutions. The calculations are also extended further downstream along the parabolic body surface by using a multizone approach with $560 \times 120$ grid points. The grid lines are stretched in both the streamwise and wall-normal directions to maintain a good resolution in the high-shear regions inside the boundary layer and near the stagnation line. The numerical accuracy of the solutions is evaluated by a grid refinement study for both the steady and unsteady solutions. Examples of the results are presented in Appendix B of this paper. Details of the numerical method and validation can be found in Zhong (1998).

## 4. Steady flow solutions

Steady solutions of the Navier–Stokes equations for viscous hypersonic flows over a parabola are obtained by using a fifth-order explicit unsteady computer code (Zhong 1998). A parabolic bow shock with a uniform flow field behind the shock is used as the initial conditions for steady flow computations. The simulations are advanced in time with fixed free stream flow conditions until the solutions between the shock and the body converge to steady states. By using the high-order shock-fitting scheme, we are able to obtain highly accurate mean flow solutions, which are free of spurious numerical oscillations behind the bow shock, for subsequent unsteady calculations.

Hypersonic flow fields over a blunt leading edge consist of three main regions as shown in figure 3. Region I is a rotational inviscid outer field, where vorticity is generated by the curved bow shock according to Crocco's theorem. Region II is a viscous stagnation flow region, where the boundary layer thickness is constant for incompressible flow and is near constant for compressible flows. Region III is the boundary layer flow downstream where boundary layer thickness grows in the streamwise direction.

Figure 4 shows the steady pressure contours and pressure distributions in both the wall-normal and the streamwise directions. The steady flow conditions are the same as those of case A.1 but with no free-stream disturbance. The $i$ indices of the grid lines in the figure are between 1 and 151, where $i = 1$ is located at the stagnation line. The
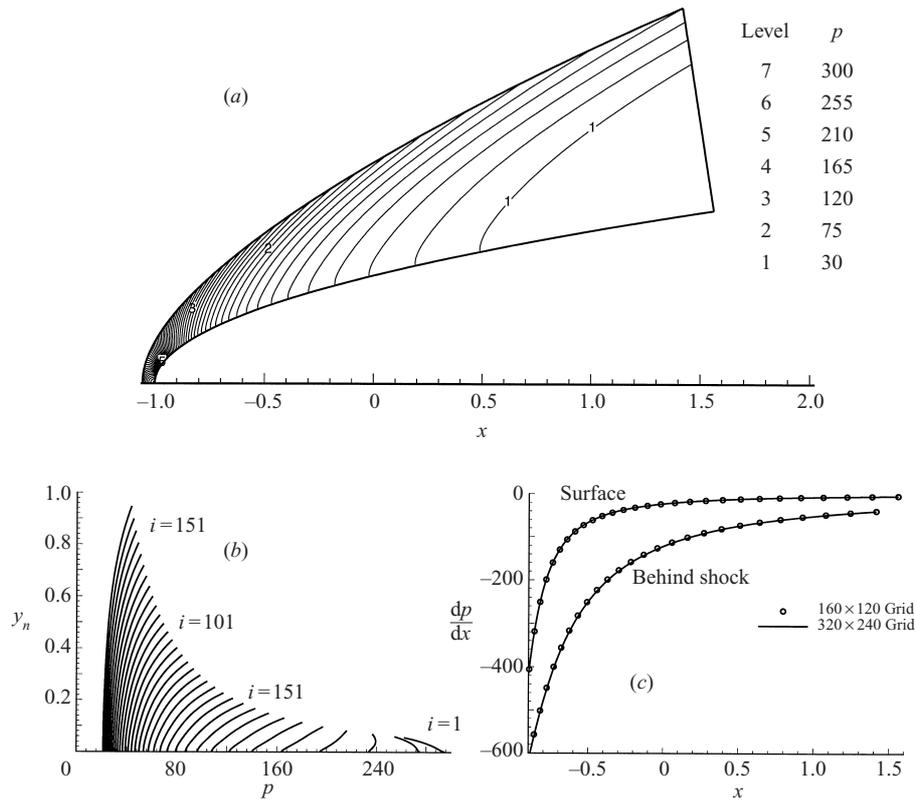
FIGURE 4. Steady pressure solutions: (a) flow field contours, (b) distribution along wall-normal grid lines for a number of grid stations, and (c) distributions of pressure gradient $dp/dx$ along the body surface and behind the bow shock ($i = 1, 51, 101, 151$ correspond to $x = -1.0, -0.693, -0.0181, 1.033$ respectively).

$x_s$ coordinates of the grid-line intersecting points on the body surface are given in the figure. The figure shows that the steady flow over the parabola develops a favourable pressure gradient along the body surface. The magnitudes of the negative pressure gradients on the body surface decrease as the flow moves downstream. Owing to the effects of nose bluntness, the pressure has a slight variation across the boundary layer in the region near the leading edge. The pressure distribution across the boundary layer approaches a constant as the flow develops further downstream.

Figure 5 shows the wall-normal distributions of tangential and normal velocities, and $\rho(du_t/dy_n)$ related to the generalized inflection point. The velocity distribution across the boundary layer is very different from a hypersonic boundary layer over a flat plate. Specifically, the velocity and other flow variables do not reach constant asymptotic states outside the boundary layer, and the normal velocity components $u_n$ are about 10% of the tangential velocity $u_t$ at the edge of the boundary layer. In addition, the $u_t$ distributions are inflectional in the region near the leading edge. For compressible flat-plate boundary layers, Lees & Lin (1946) showed that the existence of a generalized inflection point is a necessary condition for inviscid instability. The generalized inflection point is located at $d(\rho\, du/dy_n)/dy = 0$. Figure 5(b) shows that when $i \leqslant 80$ ($x = -0.355$ on the surface), there is only one generalized inflection point near the wall. As $i$ increases, an additional zero of the derivative of $d\,(\rho\, du_t/dy_n)/dy_n$
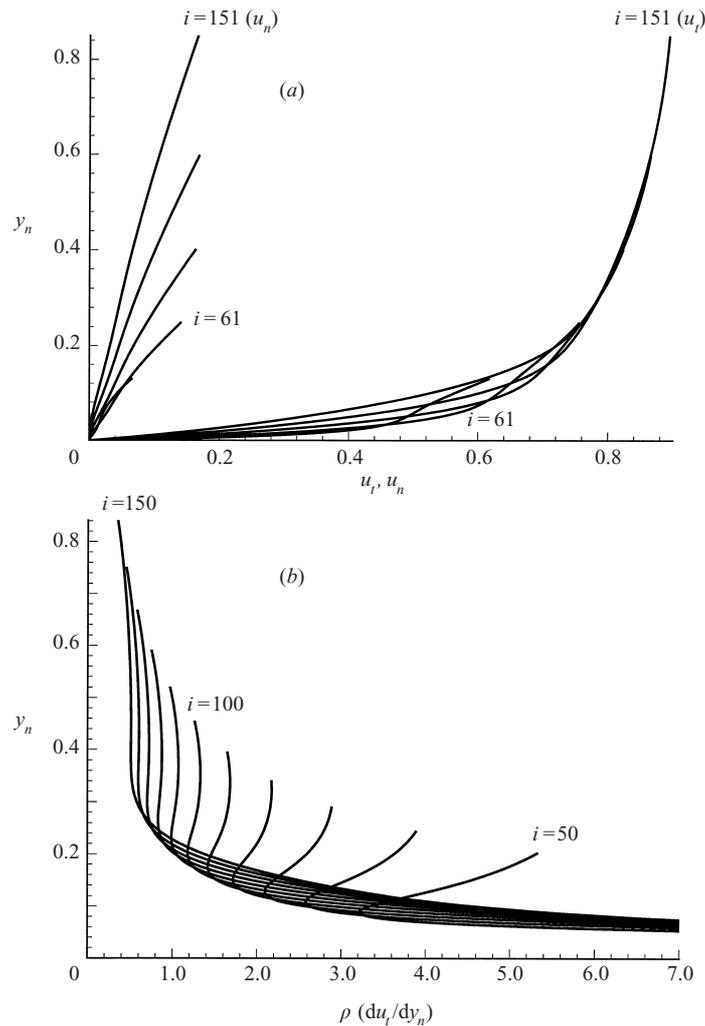
FIGURE 5. Variation of tangential velocity ($u_t$), normal velocity ($u_n$), and generalized velocity gradient $\rho\,\mathrm{d}u_t/\mathrm{d}n$ along grid lines normal to the parabola surface at several grid stations. ($i = 50, 61, 100, 150$ correspond to $x = -0.702, -0.590, -0.0362, 1.189$ respectively).

appears in the outer region of the boundary layer. At the same time, the main generalized inflection point moves further away from the wall as $i$ increases. The peak in the plots for $\rho\,\mathrm{d}u_t/\mathrm{d}y_n$ is a result of the interaction between the vorticity generated in the boundary layer in region III and the vorticity generated by the bow shock in the external rotational flows in region I.

According to Crocco's theorem, a curved bow shock generates an entropy gradient and an inviscid vorticity field behind the shock in region I. The vorticity field immediately behind the bow shock can be analysed by making an inviscid assumption for flow near the shock. The vorticity jump condition across a bow shock was derived by Truesdell (1952) using the Rankine–Hugoniot relations and Crocco's theorem or the momentum equation in the direction normal to the shock. For a bow shock in a uniform free stream, the vorticity vector behind the shock depends only on the
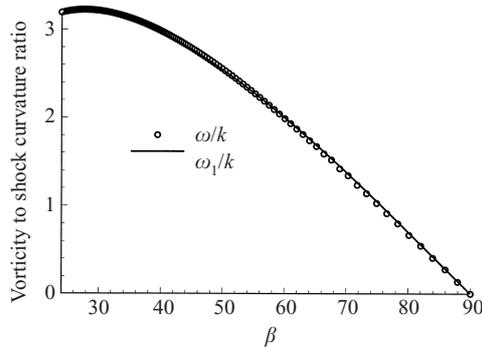
FIGURE 6. Vorticity to shock curvature ratio immediately behind the bow shock as a function of the local shock angles ($\omega/k$: numerical solutions of the Navier–Stokes equations; $\omega_1/k$: theoretical prediction).

density ratio across the shock and the shock curvature, i.e.

$$\omega_{\text{shk}}^* = u_{t\infty}^* \, k^* \, \frac{(1 - \rho_\infty^*/\rho_s^*)^2}{\rho_\infty^*/\rho_s^*} \tag{15}$$

where $\omega_{\text{shk}}^*$ is the local vorticity immediately behind the shock, $k^*$ is the shock curvature, and $u_t^*$ is the local tangential velocity component.

Equation (15) shows that the ratio of the vorticity immediately behind the bow shock to the shock curvature, $\omega_{\text{shk}}/k$, is a function of local shock angle $\beta$, $M_\infty$, and $\gamma$ only. Figure 6 compares the vorticity to shock curvature ratio as a function of local shock angle $\beta$ between the steady Navier–Stokes solution and the inviscid theoretical results of (15). The two sets of results agree very well. A close examination of the figure shows that there are slight differences in the distribution near the leading edge, which is located at $\beta = 90°$. The differences are caused by the fact that at those locations there are slight viscous effects which are not accounted for by (15). The vorticities behind the bow shock are in the negative $z$-direction. The vorticity generation by the bow shock is a function of free stream Mach number and $\gamma$.

The bow shock generates curved streamlines behind it. The streamlines immediately behind the shock are concave at points near the stagnation line, but the streamlines at the shock become convex at locations further away from the stagnation line. The ratio of streamline curvature at the shock to the shock curvature at the same points was found by Hornung (1998) to be a function of local shock angle, Mach number and $\gamma$ only, i.e.

$$\frac{k_{\text{streamline}}}{k_{\text{shk}}} = f(\beta, M_\infty, \gamma). \tag{16}$$

Figure 7 compares the streamline to shock curvature ratios between numerical solutions of the Navier–Stokes equations and the theoretical results given by (16). The two sets of results compare very well with each other. The curvature ratio is zero at the stagnation line ($\beta = 90°$) because the streamline curvature is zero. The ratios are negative near the stagnation point because the streamlines there are concave. As $\beta$ decreases, the ratios pass through the zero curvature point and become positive further downstream.

Figure 8 shows steady vorticity solutions along the body surface and behind the bow shock. The vorticity along the body surface is generated by the viscosity in the boundary layer, while the vorticity behind the shock is generated by shock curvature.
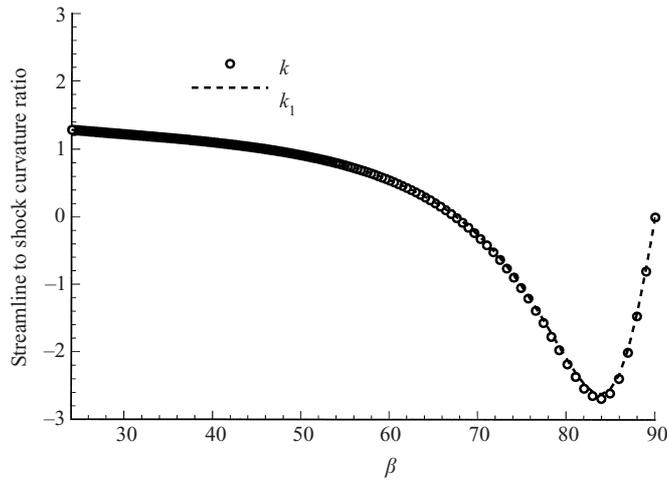
FIGURE 7. Streamline to shock curvature ratio as a function of local shock angles ($k$: numerical solutions of the Navier–Stokes equations; $k_1$: theoretical results by Hornung 1998).
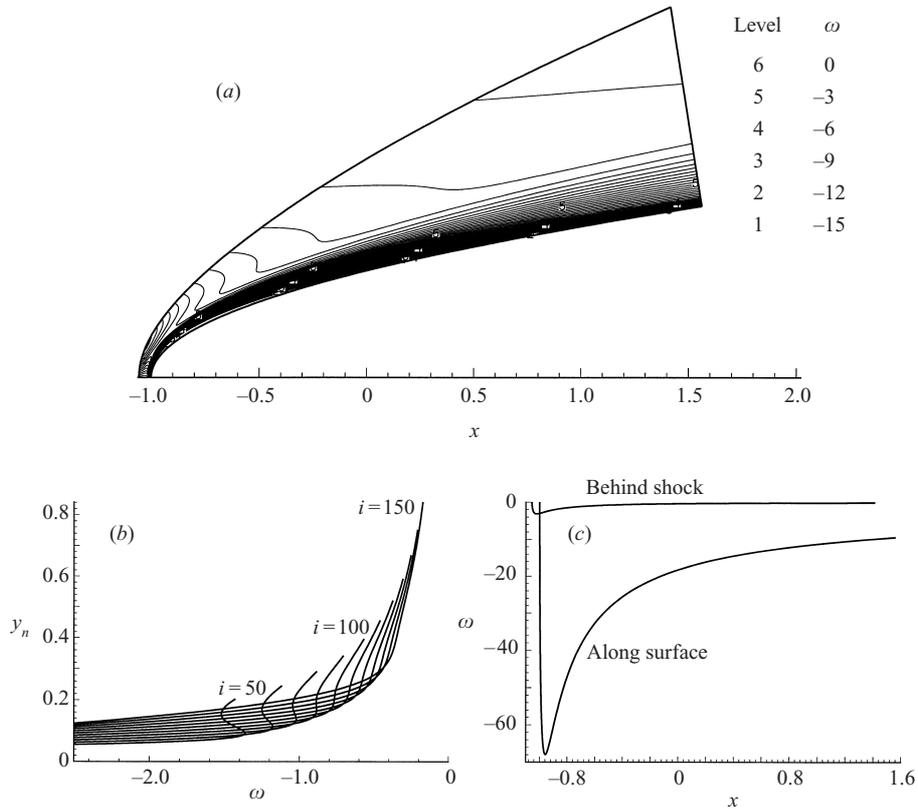


FIGURE 8. Steady vorticity solutions: (*a*) flow field contours, (*b*) vorticity distribution along wall-normal grid lines for range of $i$ grid stations, and (*c*) vorticity distribution along the body surface and behind the bow shock.

The intensity of the vorticity interaction can be characterized by the ratio of maximum vorticity magnitudes behind the shock ($\omega_{\mathrm{shk}}$) and on the body surface ($\omega_{\mathrm{wall}}$). For the present computational case, the ratio is found to be $\max(\omega_{\mathrm{shk}})/\max(\omega_{\mathrm{wall}}) = 4.65\%$, which indicates a weak vorticity interaction between regions I and III. According to (15), the vorticity behind the shock becomes stronger when the density ratio across the shock decreases. Since the limiting value of the density ratio at an infinitely strong shock is $\rho_\infty^*/\rho_s^* \to (\gamma-1)/(\gamma+1)$, it is expected that the vorticity interaction is stronger when $\gamma$ is very close to 1 because the density ratio across the shock is very small. This is the case for hypersonic flows with real gas effects. Figure 8($a$, $b$) also shows that the vorticity profiles are inflectional at the edge of the viscous boundary layer. The inflectional profiles are created by the combined effects of the vorticity in region I and in the viscous region III. It is also found that as $Re_\infty$ increases, the effects of vorticity interaction become weaker because the vorticity in the boundary layer increases while the vorticity generated by the bow shock is not affected very much by the Reynolds numbers.

The current numerical solutions of the Navier–Stokes equations are compared with approximate analytical boundary-layer equation results in order to partially validate and to better understand the numerical simulation results. The numerical study of the receptivity flow properties ultimately relies on the full Navier–Stokes solutions. These are independent of the approximate analytical solutions, and are obtained with no approximation beyond the gas models discussed in §2.

An approximate local similarity solution of the boundary layer can be obtained by using a standard similarity transformation, i.e.

$$\xi^* = \int_0^{s^*} \rho_e^* u_e^* \mu_e^* \mathrm{d}s^*, \tag{17}$$

$$\eta = \frac{u_e^*}{\sqrt{2\xi^*}} \int_0^{n^*} \rho_e^* \mathrm{d}n^*, \tag{18}$$

where $s^*$ and $n^*$ are the local dimensional natural coordinates defined by the surface length and the distance in the wall-normal direction, respectively. Subscript $e$ denotes flow variables at the edge of the boundary layer. The variable $\eta$ is the similarity coordinate across the boundary layer.

The parameters $\rho_e^*$, $u_e^*$, and $\mu_e^*$ are the dimensional density, tangential velocity, and viscosity coefficient for inviscid flow on the wall, and they are used as free-stream boundary conditions for the boundary-layer equations. For hypersonic flow over a parabola, the boundary-layer edge conditions could be obtained from inviscid solutions by computing the Euler equations. Since the pressure does not change very much across the boundary layers, we use the surface pressure obtained by the Navier–Stokes equations as the approximate edge inviscid pressure $p_e$ for boundary-layer calculations. The other inviscid conditions on the surface are obtained by an isentropic relation along the inviscid stagnation streamline.

Boundary-layer solutions in regions II and III are obtained by using an approximate local similarity solution by assuming $u^*/u_e^* = f(\eta)$ and $T^*/T_e^* = g(\eta)$. Substituting these new variables into the compressible boundary-layer equations, and neglecting the effects of body surface curvature, leads to the following standard similarity equations:

$$(Cf'')' + ff'' + \alpha(g - f'^2) = 0, \tag{19}$$

$$\left(\frac{C}{Pr}g'\right)' + fg' + (\gamma-1)M_e^2 Cf''^2 = 0, \tag{20}$$
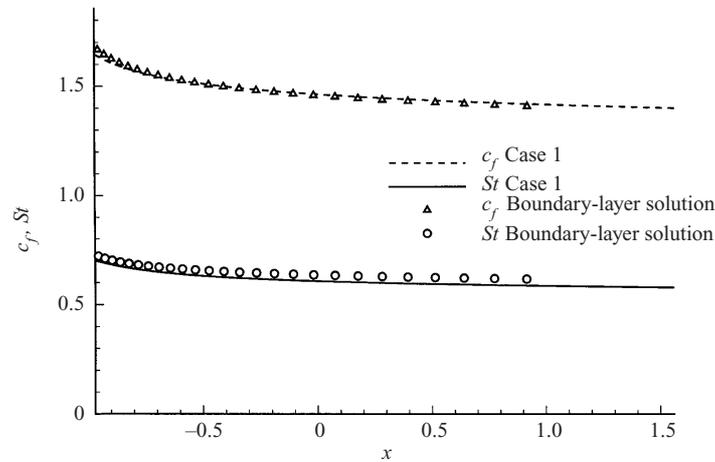
FIGURE 9. Distributions of locally defined skin friction coefficients $c_f$ and heat transfer coefficients $St$ along the body surface (Case 1: Case A).

where $C = \rho^* \mu^* / (\rho_e^* \mu_e^*)$ is the Chapman–Rubesin parameter, $M_e$ is the edge Mach number, and

$$\alpha = \frac{2\xi^*}{u_e^*} \frac{\mathrm{d} u_e^*}{\mathrm{d}\xi^*}$$

is the edge velocity gradient parameter. This nonlinear set of ordinary differential equations with appropriate boundary conditions is solved by a shooting method based on a fourth-order Runge–Kutta scheme. Although great simplifications have been made in the boundary layer solutions, the results show that these local similarity solutions are surprisingly accurate for hypersonic flow over a parabola, as long as the surface pressure is known.

The Navier–Stokes solutions and independently obtained boundary-layer similarity solutions for the same flow conditions are compared by normalizing the Navier–Stokes solutions by local boundary-layer edge parameters. Figure 9 shows a local shear stress coefficient $c_f$ and Stanton number $St$ defined by local boundary layer variables, i.e.

$$c_f = \frac{\tau_w^*}{\rho_e^* u_e^{*2}/2} \sqrt{\frac{2\xi^*}{\mu_e^{*2}}} \quad \text{and} \quad St = \frac{q_w^*}{\rho_e^* u_e^* (h_{0e}^* - h_w^*)} \sqrt{\frac{2\xi^*}{\mu_e^{*2}}}. \tag{21}$$

The Navier–Stokes solutions agree well with the boundary-layer results for both skin friction and heat transfer rates. The results also show that there is a characteristic of $c_f$ and $St$ similar to the Reynolds analogy in flat-plate boundary layers, in that $c_f/(2St)$ is close to a constant, near 1.14 for the current flow conditions.

The interaction of solutions in regions I and III can be shown by plots of tangential velocity $u^*/u_e^*$ vs. boundary-layer coordinate $\eta$ along wall-normal grid lines. Figure 10 compares velocity profiles of the boundary-layer similarity solutions with those of the Navier–Stokes solutions for two different Reynolds numbers. In the figure, $i = 12$ ($x = -0.974$ on the surface) is a grid line near the nose region while $i = 127$ ($x = 0.539$ on the surface) is located further downstream. The results show a good agreement among the three sets of profiles near the wall up to the edge of the boundary layer located approximately at $\eta = 3$. The velocity profiles are nearly independent
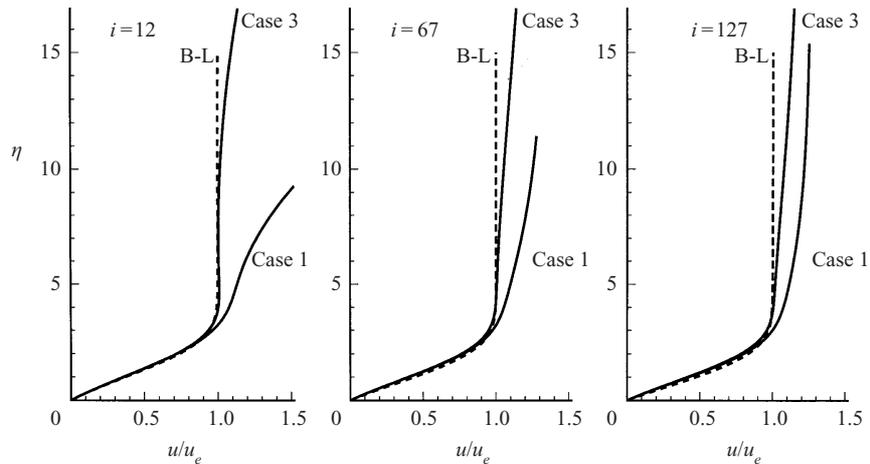
FIGURE 10. Distributions of streamwise velocity components along wall-normal grid lines for three $i$ grid stations as functions of local boundary layer similarity coordinates $\eta$ (Case 1: $Re_\infty = 6026.6$; Case 3: $Re_\infty = 60\,266$; B-L: boundary layer solutions).

of Reynolds number when the velocities are normalized by local boundary-layer similarity parameters. The Navier–Stokes velocity profiles have an inflection point near the leading edge due to strong inviscid vorticity outside the boundary-layer. As the flow moves downstream, the velocity profiles become fuller and approach the boundary-layer similarity solutions.

## 5. Receptivity to free-stream acoustic waves

The first group of cases (case A) is the receptivity simulations involving free-stream planar acoustic waves. The unsteady flow solutions are obtained by imposing acoustic disturbances on the steady flow solutions in the free stream. The subsequent interaction of the disturbances with the shock and the receptivity of the boundary layer over the parabola are computed by using the full Navier–Stokes equations. The flow conditions of the computational cases are given in Appendix A for seven values of $F$ ranging from 531 to 2655, corresponding to the Strouhal numbers ranging from 0.4 to 2.0. Unless stated explicitly, we present the results for case A.1 with $F = 2655$ and $\epsilon = 5 \times 10^{-4}$.

### 5.1. *Wave field structure*

Figure 11 shows the contours of instantaneous perturbations $u'$ and $v'$, after the flow field reaches a time-periodic state. The instantaneous contours show the interaction of the free-stream disturbances with the bow shock and the development of disturbance waves in the boundary layer on the surface. The wave patterns in region I outside the boundary layer are different from those in region III inside the boundary layer: in region I they are the result of free-stream waves passing through the shock and propagating in the flow field; in region III they are dominantly the boundary-layer waves induced by the forcing waves.

The wave field behind the bow shock is a combination of the external forcing disturbance waves, Stokes-wave solutions, and boundary-layer waves. In a receptivity study of an incompressible boundary layer, the wave field is a combination of a T–S wave induced by the receptivity process and a Stokes solution in response

| Level | $u'$ |
|---|---|
| 6 | 0.003 |
| 5 | 0.0018 |
| 4 | 0.0006 |
| 3 | −0.0006 |
| 2 | −0.0018 |
| 1 | −0.003 |

| Level | $v'$ |
|---|---|
| 6 | 0.002 |
| 5 | 0.0012 |
| 4 | 0.0004 |
| 3 | −0.0004 |
| 2 | −0.0012 |
| 1 | −0.002 |
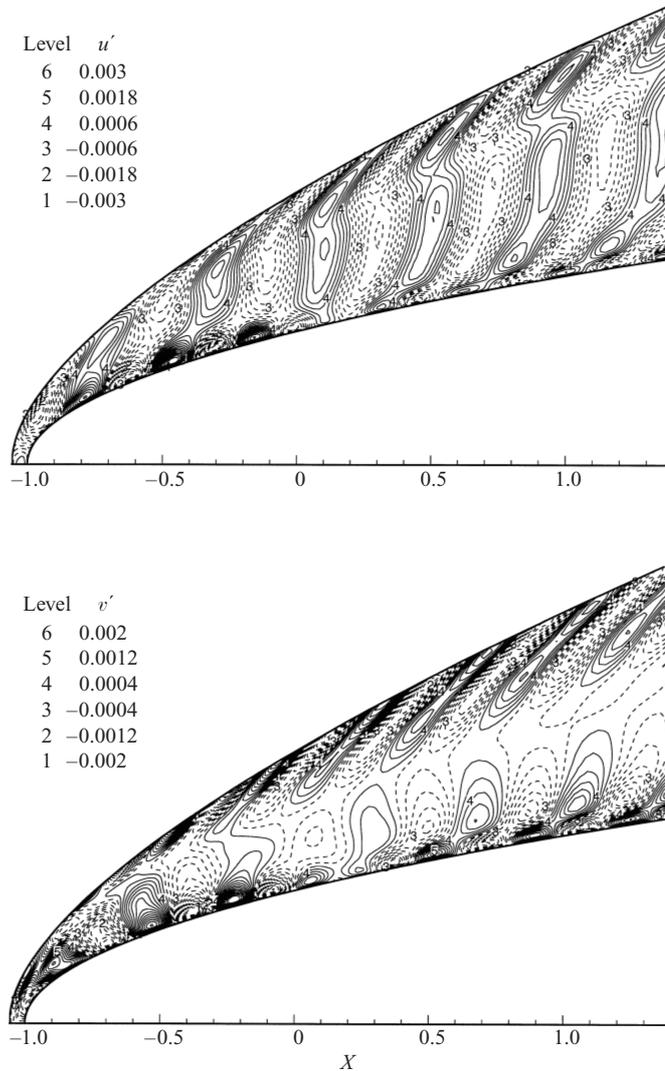
FIGURE 11. Contours of instantaneous perturbations of velocity components ($u'$ and $v'$) after the unsteady solutions reach a time-periodic state for case A.1 at $\epsilon = 5 \times 10^{-4}$.

to the forcing waves. The components of the T–S wave can be separated (Buter & Reed 1994) from the Stokes-wave solutions by recognizing that the free-stream wavelengths are an order of magnitude longer than those of the T–S waves in the boundary layers. For hypersonic boundary layers, however, such separation is not possible because the wavelengths of the forcing waves in the free stream are of the same order of magnitude as those of the disturbance waves in the boundary layers. Figure 11 shows the wavelengths of the disturbance waves developed in the boundary layer to be very close to those of the external waves at the bow shock. In addition, the disturbance wave field behind the shock is very complex due to the back and forth reflection of the acoustic waves in the region between the bow shock and the body. Though we cannot separate the external waves from the boundary layer wave modes in hypersonic receptivity studies, figure 11 shows that the waves inside the boundary
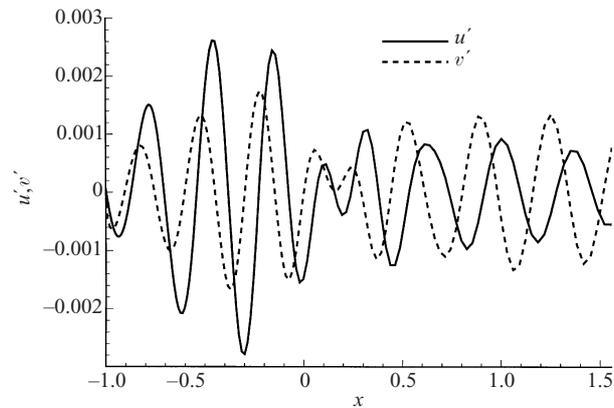
FIGURE 12. Distribution of instantaneous perturbations of velocity components in the boundary layer along the $j = 30$ grid line near the body surface for case A.1 at $\epsilon = 5 \times 10^{-4}$.
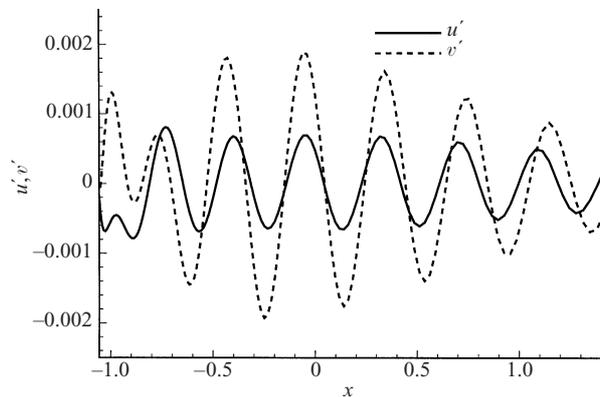


FIGURE 13. Distribution of instantaneous perturbations of velocity components immediately behind the shock for case A.1 at $\epsilon = 5 \times 10^{-4}$.

layer near the body surface are dominantly boundary-layer waves, while the waves immediately behind the bow shock are mainly external forcing waves.

The waves in the boundary layer region on the wall, as shown in figure 11, contain two separate zones of different wave patterns. The first zone is located in the region $x < 0.2$ and the second in $x > 0.2$. In the first zone, there is only one peak in the oscillation magnitude across the boundary layer. On the other hand, in the second zone oscillations develop away from the wall with two peaks. It is shown later in this paper that the waves in the first wave zone correspond to the first-mode waves, while those in the second zone are dominated by the second-mode waves. This will be confirmed by comparing the eigenfunctions of the first and second modes obtained by a local linear stability analysis with the numerical solutions of the Navier–Stokes equations.

The instantaneous wave field development along the body surface is shown in figure 12, for the variation of velocity perturbations along a parallel grid line near the body surface. The instantaneous profiles, on the body surface, of other variables are similar, in terms of the growth and decay of wave patterns, to those in this figure. It shows two main distinct wave zones inside the boundary layer. However,
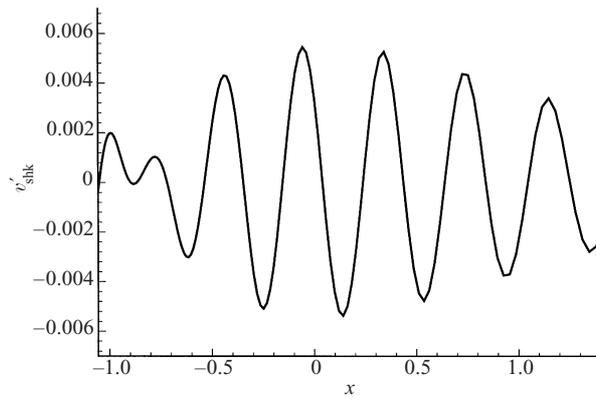
FIGURE 14. Distribution of instantaneous perturbations of normal shock velocities vs. $x$ for case A.1 at $\epsilon = 5 \times 10^{-4}$.
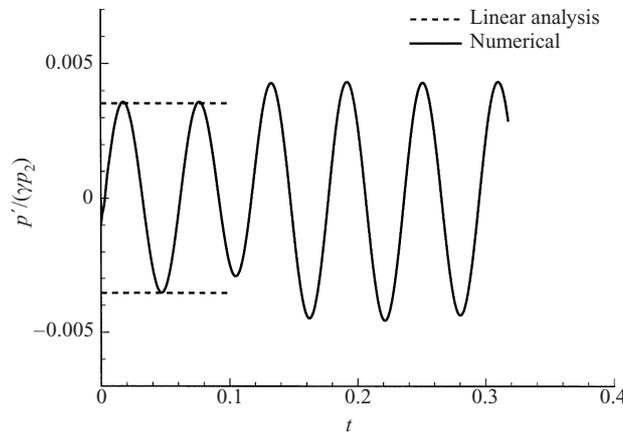


FIGURE 15. Time history of the instantaneous pressure perturbations at the point immediately behind the bow shock at the centreline for the case $F = 7080$ at $\epsilon = 5 \times 10^{-4}$.

the change of wave modes does not exist in region I which is outside the boundary layer. Figure 13 shows the distribution of instantaneous perturbations of velocity components immediately behind the bow shock. There is only a single wave pattern in the solution behind the bow shock, which is outside the boundary layer.

In an unsteady flow simulation, the bow shock oscillates due to perturbations by free-stream disturbances and by the reflection of acoustic waves from the boundary layer to the shock. Figure 14 shows the numerical results for instantaneous perturbations of normal shock velocities vs. $x$ for case A.1. Positive normal shock velocities represent shock movements in the direction opposite to the free-stream mean velocity. There is no different wave mode of unsteady motion at the shock, which is outside the boundary layer. The wavelength of the shock velocity is the same as that of the disturbances in the free stream. Figure 12 shows that the wavelengths of disturbance waves on the wall are very close to that of the forcing wave in the free stream.

One way to check the accuracy of the numerically computed unsteady shock/ disturbances interaction is by a comparison with linear theory of shock/disturbance interaction. Figure 15 shows the time history, starting from $t = 0$, of the instantaneous pressure perturbations at a point immediately behind the bow shock at the centreline

for the case of $F = 7080$. A relatively higher frequency case is used here so that the initial shock oscillates for a complete period in time before the acoustic wave reflection from the wall returns and interacts with the bow shock. At the initial moment of imposing the free-stream disturbances, there are no reflected waves from the undisturbed steady boundary layer. The linear interaction of a free-stream disturbance wave with a planar shock can be predicted by a linear theory such as that derived by McKenzie & Westphal (1968). For the case of the transmission of a free-stream acoustic wave through a normal shock,

$$\frac{|p'_s|}{|p'_\infty|} = \frac{2M_\infty^4 + 2(\gamma + 1)M_\infty^3 + 2(3\gamma - 1)M_\infty^2 + 1 - \gamma}{(\gamma + 1)(1 + M_\infty^2 + 2M_\infty^2 M_s)}, \tag{22}$$

where $|p'_\infty|$ and $|p'_s|$ are amplitudes of pressure perturbations in the free stream and immediately behind the shock respectively. This prediction is valid for weak free-stream waves until a later time ($t \approx 0.1$ for the case of $F = 7080$). After $t \approx 0.1$, the wave amplitudes of the pressure perturbations in the numerical simulation change because the disturbance waves generated at the shock enter the boundary layer and generate reflected waves back to the shock. Figure 15 shows very good agreement between the numerical simulation results and the linear predictions for the pressure perturbation when they are assumed to agree with each other at the initial moment of the simulation.

## 5.2. *Wave amplitudes and phase angles*

Temporal Fourier analysis is carried out on the numerical solutions of the perturbations of unsteady flow variables after a time-periodic state has been reached in a simulation. A Fourier transform of a disturbance variable leads to

$$q'(x, y, t) = \mathrm{Re} \left\{ \sum_{n=0}^{N} |q'_n(x, y)| e^{i[-n\omega t + \phi_n(x,y)]} \right\}, \tag{23}$$

where $\omega$ is the forcing frequency of the acoustic wave in the free stream, $q'(x, y, t)$ represents any instantaneous perturbation variables, and $|q'_n(x, y)|$ and $\phi_n(x, y)$ are the local perturbation amplitude and phase angle respectively. The integer $n$ represents the wave modes of the perturbation fields, where $n = 0$ is the mean flow distortion, $n = 1$ is the fundamental mode, and $n = 2$ is the second harmonic, etc. $\phi_n(x, y)$ indicates a local phase angle with respect to the forcing wave in the free stream. If the wave modes in the boundary layer on the body surface are dominated by a single wave mode, a local growth rate $\alpha_r$ and a local wavenumber $\alpha_i$ of a perturbation field of the fundamental frequency can be defined by

$$\alpha_i = \frac{1}{|q'_1|} \frac{\mathrm{d}|q'_1|}{\mathrm{d}s}, \quad \alpha_r = \frac{\mathrm{d}\phi_1}{\mathrm{d}s}, \tag{24}$$

where the derivatives are taken along a parallel grid line near the body surface.

Figure 16 shows the contours of Fourier amplitudes and phase angles of the horizontal velocity components $u'$ for $F = 2655$. The amplitude contours show a strong growth near the leading edge in the boundary layer on the wall, followed by a rapid decay and transition to another wave mode. This is shown quantitatively in figure 17 for the amplitude distribution of the velocity perturbations near the parabola surface. These figures show two distinct main zones of first- and second-mode waves. The first mode is much stronger than the second mode for the current test case. The

Level $\phi_u$
6    329.0
5   −291.5
4   −912.1
3   −1532.6
2   −2153.1
1   −2773.6

Level $u$
7   0.00297
6   0.002475
5   0.00198
4   0.001485
3   0.00099
2   0.000495
1   0

$x$
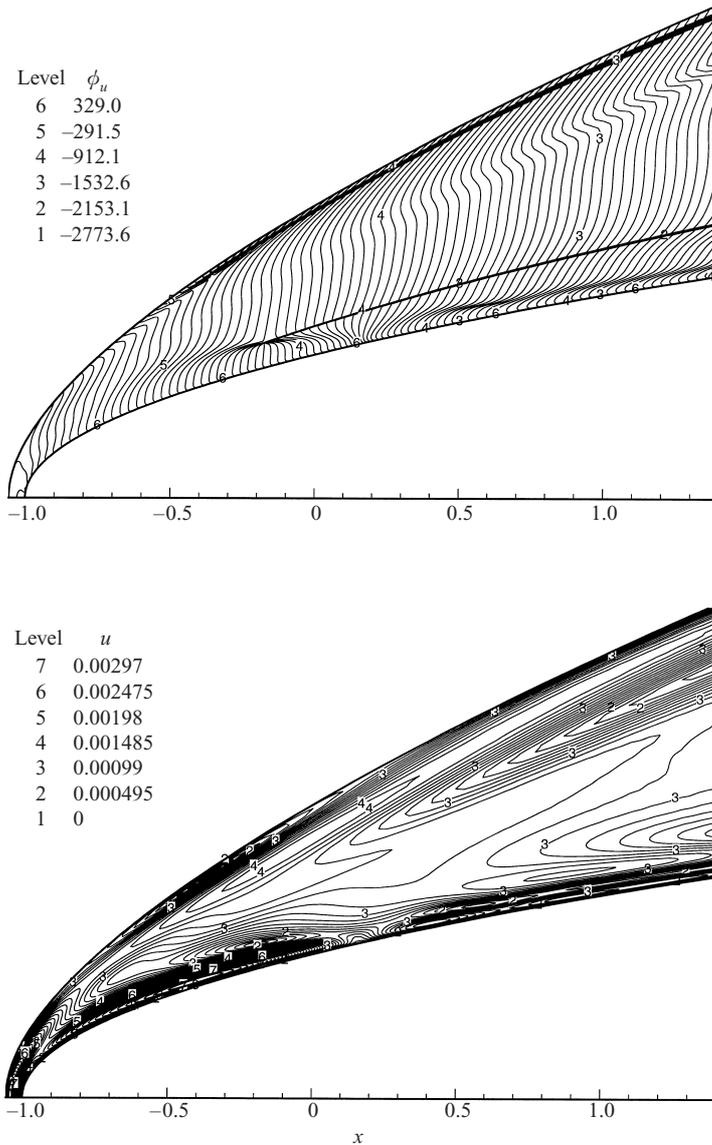
FIGURE 16. Contours of Fourier amplitudes and phase angles (in degrees) of horizontal velocity components $u'$ for case A.1 at $\epsilon = 5 \times 10^{-4}$.

transition of wave modes from the first zone to the second occurs at about $x = 0.2$ on the surface. Though not presented here, all other perturbation variables show similar growth and decay characteristics inside the boundary layer. The propagation of the perturbation waves is represented by the spatial distribution of lines of constant phase angles shown in figure 16. Note that some of the discontinuous contour lines in the phase angle contours with jumps in multiples of $360°$ are not real discontinuities for phase angles. The decay of the first mode and the growth of the second mode is shown by a sudden phase change near the body surface around $x = 0.2$. The phase structure has one more variation across the boundary layer after the change of modes.

The variation of amplitude of tangential velocity perturbations along grid lines
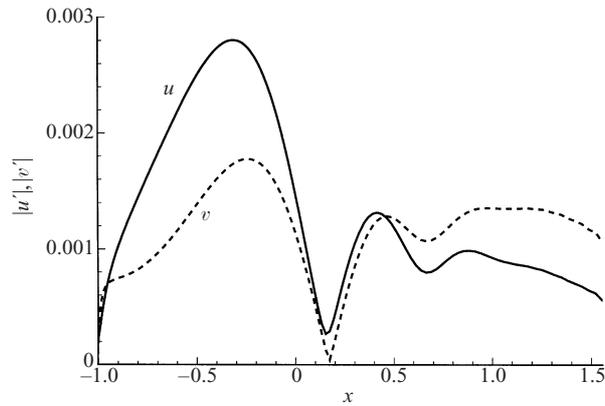
FIGURE 17. Distribution of the Fourier amplitudes of the velocity perturbations in the boundary layer along the $j = 30$ grid line near the parabola surface for case A.1 at $\epsilon = 5 \times 10^{-4}$.
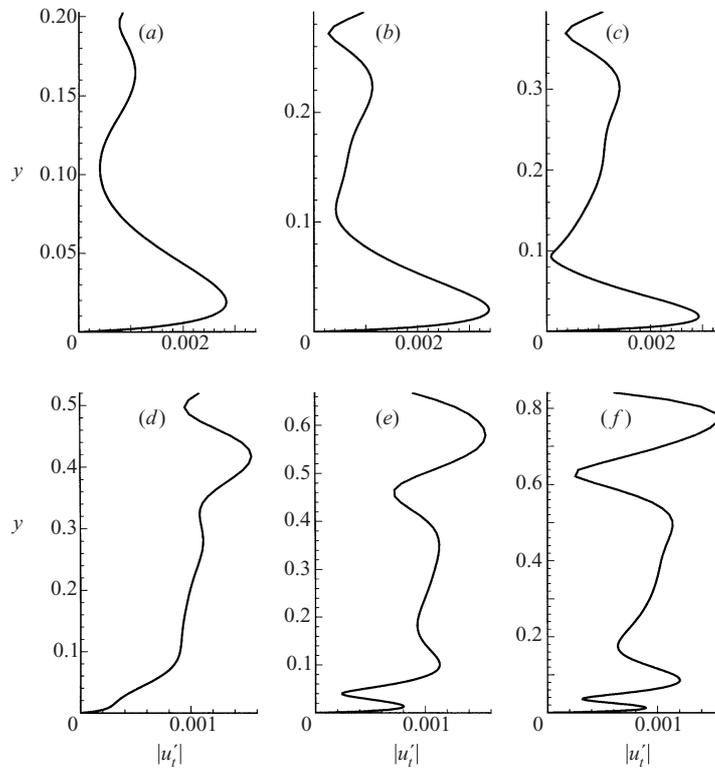


FIGURE 18. Variation of amplitudes of tangential velocity perturbations along grid lines normal to the parabola surface at several wall-normal grid stations for case A.1 at $\epsilon = 5 \times 10^{-4}$. (a) $x = -0.702$, (b) $x = -0.486$, (c) $x = -0.206$, (d) $x = 0.155$, (e) $x = 0.614$, (f) $x = 1.189$.

normal to the parabola surface at several grid stations is shown in figure 18. The first three stations (a–c) are located in the first wave zone of the first mode, station (d) is located in the mode switching zone, and the last two stations (e) and (f) are located in the second wave zone of the second or third modes. The figure shows different amplitude structures inside the boundary layer for the two wave zones. Mack (1984)
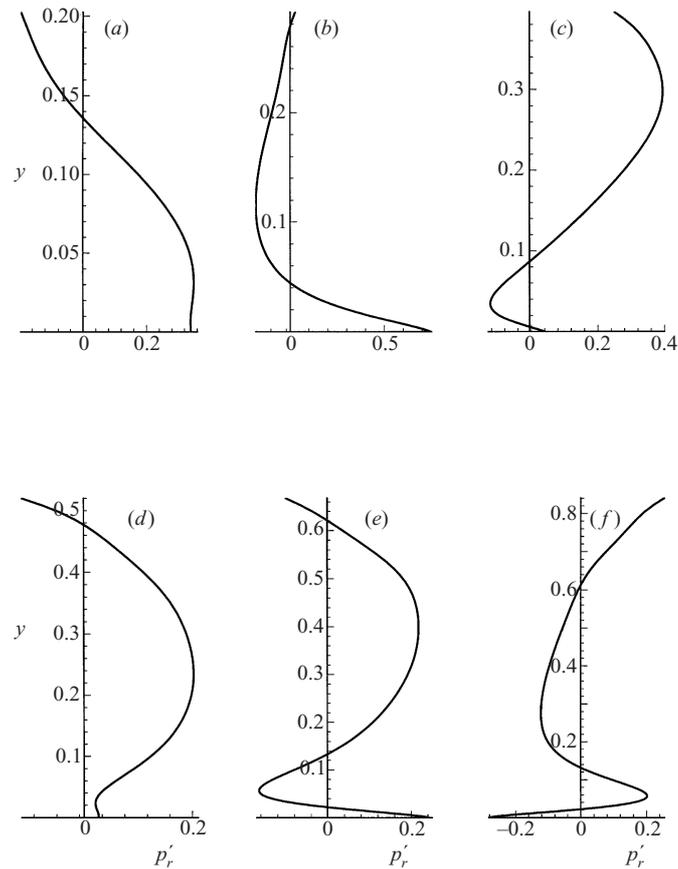
FIGURE 19. Variation of the real part of the Fourier transform for the pressure perturbations along grid lines normal to the parabola surface at several wall-normal grid stations for case A.1 at $\epsilon = 5 \times 10^{-4}$. (*a*) $x = -0.702$, (*b*) $x = -0.486$, (*c*) $x = -0.206$, (*d*) $x = 0.155$, (*e*) $x = 0.614$, (*f*) $x = 1.189$.

defined the first, second, and third modes of a supersonic boundary layer on a flat plate by the structure of the real part of the eigenfunctions of pressure perturbations. The number of zeros in the eigenfunctions was used by Mack to identify the mode numbers for compressible boundary layers. Figure 19 shows the variation of the real part of the Fourier transform for the pressure perturbations obtained by the numerical simulations for the present case A.1. The structure inside the boundary layer shows the first mode in the first wave zone and the second or even third modes in the second wave zone.

Therefore, on the body surface, first, second, and even higher modes are generated and propagate downstream along the wall. The first mode is generated near the leading edge. The amplitude of the first mode increases first and then decreases rapidly after reaching maximum values. After the first-mode decay, the second and third mode disturbances become dominant. The decay of the first mode and the growth of the second mode are shown by a sudden change of phase angle near the body surface at that location. The phase structure changes dramatically between the two modes. Specifically, the second mode has one more variation across the boundary layer.
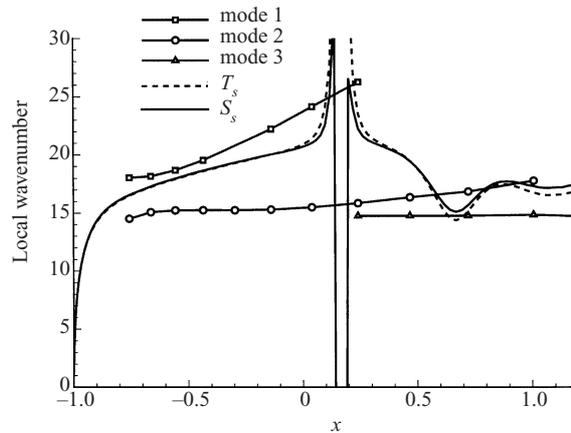
FIGURE 20. Distribution of the local wave numbers in the boundary layer along the $j = 30$ grid line near the parabola surface for case A.1 at $\epsilon = 5 \times 10^{-4}$.

### 5.3. *Comparison with linear stability analysis*

A local parallel linear stability analysis is used to compare with the numerical solutions of the Navier–Stokes equations in order to confirm the identification of the numerically obtained boundary-layer eigenmodes. Linear stability analysis is carried out using the numerically obtained steady base flow between the body and the bow shock. A spatial linear stability code, developed by Hu & Zhong (1998), based on both a fourth-order finite difference method and a spectral method is used. The disturbance equations are reduced to an eigenvalue problem by assuming that the perturbations of flow variables are in a normal-mode form, i.e.

$$q' = \hat{q}(y_n)\, e^{i(\omega t - \alpha s)}, \tag{25}$$

where $y_n$ and $s$ are coordinates along the wall-normal and the body surface directions, $\alpha$ is the wavenumber, and $\hat{q}(y_n)$ is the eigenfunction. In the linear stability analysis, $\alpha$ and $\hat{q}(y_n)$ are obtained as the eigenvalue and the eigenfunction of the stability equations for a given frequency $\omega$. For the spatial problem, $\omega$ is real, and $\alpha$ is a complex wavenumber, $\alpha = \alpha_r + i\alpha_i$, where $\alpha_r$ and $\alpha_i$ represent the spatial wavenumber and growth rate of a wave mode respectively. A linear wave mode is unstable when $\alpha_i$ is positive.

The wave modes obtained by the linear stability analysis are compared with the numerically obtained Fourier amplitudes and wavenumbers defined by (24). Since the receptivity simulation is an initial boundary value problem with non-homogeneous forcing terms in the free stream, while the linear stability analysis involves a homogeneous eigenvalue problem, it is expected that the two solutions will not agree in region I located outside the boundary layer. The comparison is used mainly to identify the wave modes obtained by the receptivity simulations. If the waves in the boundary layer consist dominantly of a single wave mode, the wavenumbers and eigenfunctions from the numerical solution should agree reasonably well with the linear stability results in region III in the boundary layer on the wall.

Figure 20 shows the local wavenumber $\alpha_r$ in the boundary layer along a grid line near the parabola surface for $F = 2655$. The receptivity solutions include the wavenumber computed using both temperature and entropy perturbations. The linear stability results for the first, second and third modes are compared with the results
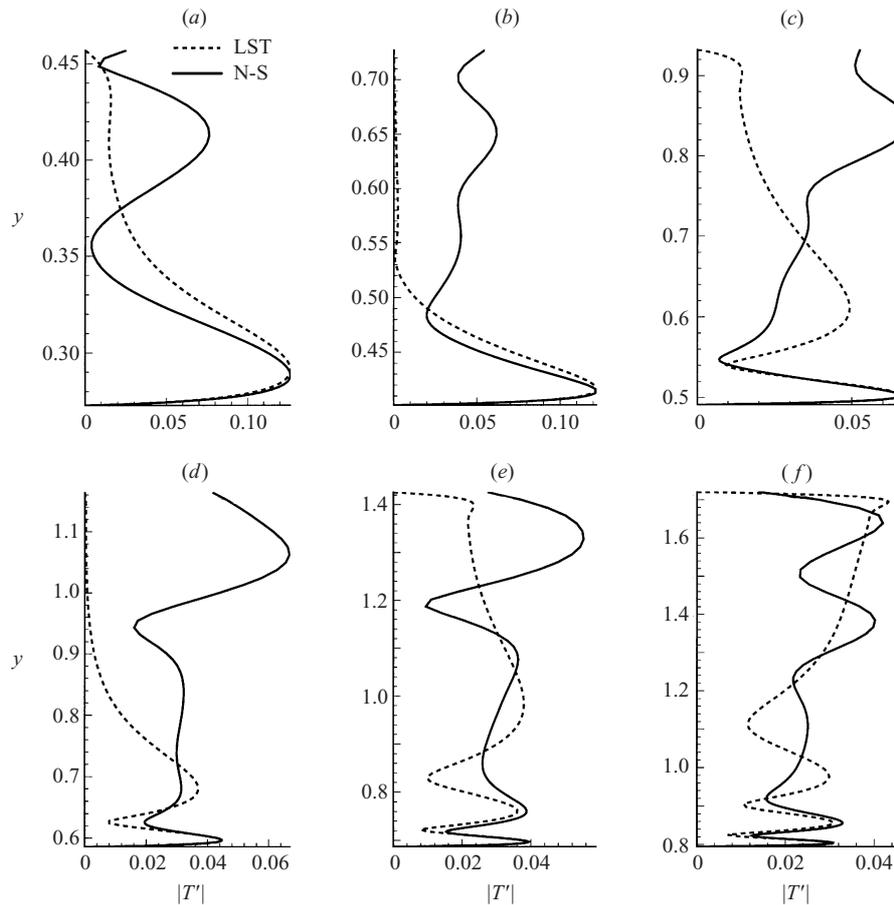
FIGURE 21. Variation of the temperature amplitudes along grid lines normal to the parabola surface at six wall-normal grid stations for case A.1 at $\epsilon = 5 \times 10^{-4}$. (*a*) $x = -0.702$ LST: 1st mode, (*b*) $x = -0.355$ LST: 1st mode, (*c*) $x = -0.0362$ LST: 2nd mode, (*d*) $x = 0.372$ LST: 2nd mode, (*e*) $x = 0.886$ LST: 3rd mode, (*f*) $x = 1.525$ LST: 3rd mode.

obtained by numerical simulations. In the first mode region, the wavenumber increases (wavelength decreases) in the $x$-direction. The figure shows that the linear stability first-mode wavenumber has the closest agreement with the numerical wave solutions in this region. The results agree reasonably well considering the fact that the linear stability analysis is based on a parallel flow assumption, while the numerical solution is obtained in a flow field which is not strictly parallel and includes the effects of surface curvature. As the waves develop downstream, there is in the simulations a gradual transition from the first mode to the second, and then to the third mode. The transition from the second to the third mode is not obvious in this figure. It is determined by comparison with the LST results instead.

The identification of the wave modes induced by free-stream disturbances is further examined by comparing the linear stability eigenfunctions with Fourier amplitudes of the Navier–Stokes solutions for the receptivity problem. For the purpose of comparison, the eigenfunctions are normalized by their respective first peak values from the wall. Figure 21 shows such comparisons for the temperature amplitudes along grid lines normal to the parabola surface at several grid stations for $F = 2655$.
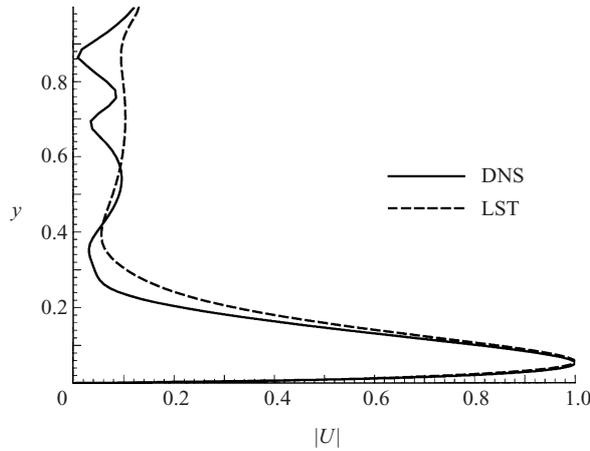
FIGURE 22. First-mode horizontal velocity eigenfunction amplitudes along the wall-normal direction at $x = 0.5521$ for case A.3 at $\epsilon = 5 \times 10^{-4}$.

The numerical solutions at earlier stations in first wave zone I of $x = -0.702$ and $x = -0.355$ agree best with the linear stability first mode inside the boundary layer near the wall, whereas at later stations, the numerical results gradually change to profiles that are closer to the linear stability second mode at $x = -0.0362$ and $x = 0.372$, and to the linear stability third mode at $x = 0.886$ and $x = 1.525$. The figure also shows that due to the effects of interaction of the bow shock with the flow disturbances, the numerical solutions have very complex flow distributions in the inviscid region I outside the boundary layer. The numerical results and linear stability results agree mainly inside the boundary layer on the wall. In the flow region I outside the boundary layer, the two solutions do not agree because the numerical solutions contain both the homogeneous wave modes and the non-homogeneous solutions induced by the forcing wave in the free stream. Therefore, the results indicate that the disturbance waves excited in the first region are dominated by the first mode, followed by a gradual transition to the second and third modes downstream.

The agreement between the linear stability wavenumbers and eigenfunctions and numerical results becomes better for lower frequencies. Figure 22 compares the linear stability first-mode eigenfunction with amplitudes of the simulation in the wall-normal direction at $x = 0.5521$ for $F = 1770$. The numerical results agree very well with the linear stability results inside the boundary layer. Again, the disagreement outside the boundary layer, near the bow shock, is expected because the effects of the forcing disturbances are not considered in the linear stability analysis.

The linear stability analysis also shows that the first mode is the least stable mode near the leading edge, while the second mode becomes the least stable mode further downstream. However, for the present test case, linear stability theory predicts stable normal modes while the numerical simulation shows rapid growth in the first-mode region near the leading edge. This is expected because the receptivity mechanism involves interaction and energy exchange of the forcing waves and the boundary-layer waves, while the LST results are based on the free development of a single wave mode. Figure 23 shows the distribution of local growth rates defined by (24) along the parabola surface for linear stability analysis and numerical simulation results for case A.1. The figure shows linear stability results predict all stable modes in the boundary layer, but the numerical simulation shows a strong growth of the first mode near the
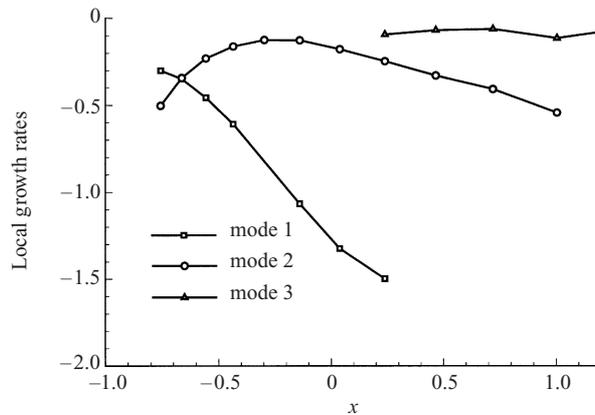
FIGURE 23. Distribution of local growth rates obtained by the linear stability analysis for the first, and second, and third modes along the $j = 30$ grid line near the parabola surface for $F = 2655$.

leading edge by the receptivity process. Such strong growth is an indication that the disturbance energy is converted to the first mode energy at the leading edge by the receptivity process even though the linear eigenmode development is stable.

For hypersonic flows over a blunt body, the interaction of the bow shock with a free-stream wave of any kind always generates a combination of all three kinds of waves: acoustic, entropy, and vorticity. All these waves propagate downstream and play a role in the receptivity of the boundary layer on the body surface. The instantaneous contours of vorticity, pressure, and entropy perturbations are plotted in figure 24 for case A.1. They are represented by pressure, vorticity, and entropy perturbations, respectively. The wave patterns generated in the boundary layer on the wall are similar for all three variables. The pressure contours show that effects of acoustic wave reflection from the wall alter the wave pattern outside the boundary layer. On the other hand, the vorticity and entropy waves are convected in the inviscid region I without reflection. The figure also shows a strong interaction between the boundary layer and the acoustic field, while the interaction of the boundary layer with entropy and vorticity fields is much weaker.

### 5.4. *Nonlinearity and superharmonics*

For weak monochromatic free-stream forcing waves, the generation of boundary-layer waves with the same fundamental frequency is expected to be linear with respect to the forcing amplitudes. Figure 25 shows the maximum temperature amplitudes of the first and second modes of the fundamental frequency as functions of disturbance amplitudes of the free stream forcing waves for case A.1. When $\epsilon$ is very small, the receptivity of the wave mode of the fundamental frequency is linear. As $\epsilon$ increases, the receptivity results deviate from the linear curves due to the nonlinear interaction between the wave harmonics.

As the forcing amplitude increases, the nonlinear receptivity effects become significant. These are a result of nonlinear interaction among the wave modes and their superharmonics. Previous receptivity and stability experiments (Stetson & Kimmel 1992) have shown the existence of higher harmonics in addition to the waves of the fundamental frequency. Buter & Reed (1994) found nonlinear superharmonics in their incompressible receptivity simulations. Nonlinear higher harmonics are also found in the present numerical simulation study. Figure 26 shows the instantaneous

Level $\omega'$
6    0.1
5    0.06
4    0.02
3   −0.02
2   −0.06
1   −0.1

Level $p'$
6    1.5
5    0.6
4   −0.3
3   −1.2
2   −2.1
1   −3

Level $s'$
6    0.006
5    0.0036
4    0.0012
3   −0.0012
2   −0.0036
1   −0.006
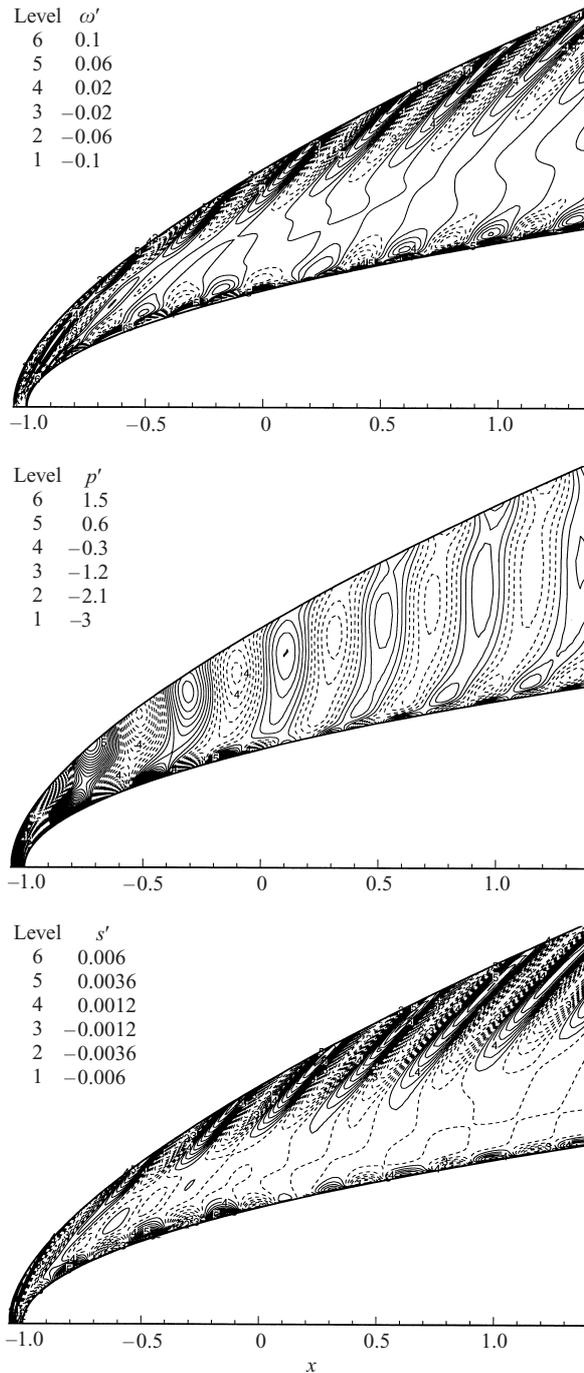
FIGURE 24. Contours of instantaneous perturbations of vorticity, pressure, and entropy for case A.1 at $\epsilon = 5 \times 10^{-4}$.

entropy disturbances along the body surface for $F = 1770$ and $\epsilon = 5 \times 10^{-4}$ for the fundamental frequency ($n = 1$) and its second harmonic ($n = 2$). Both the fundamental mode and the second harmonic are plotted in the figure, where the magnitude of the second harmonic is amplified 10 times so that the two modes can be plotted
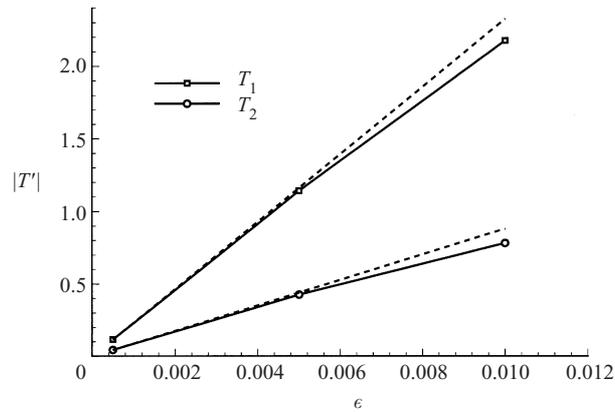
FIGURE 25. Maximum temperature amplitudes of the first mode ($T_1$) and the second mode ($T_2$) of the fundamental frequency vs. amplitudes $\epsilon$ of free stream forcing disturbances for case A.1. The dotted lines are the expected linear response to the free stream forcing amplitudes.
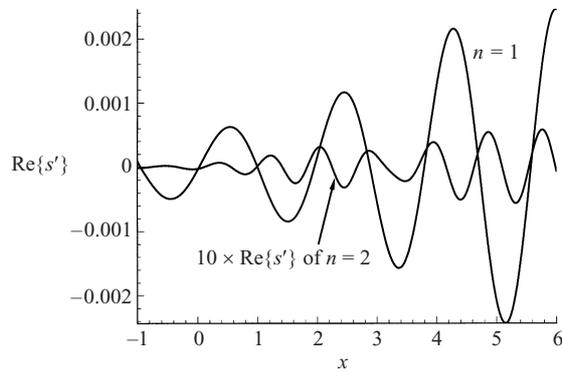


FIGURE 26. Instantaneous entropy disturbances along the body surface for case A.3, $F = 1770$ ($n = 1$: fundamental mode; $n = 2$: second harmonic).
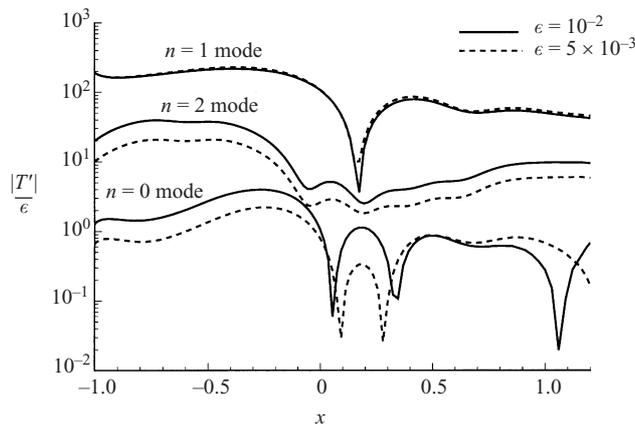


FIGURE 27. Distribution of amplitudes of temperature perturbations in the boundary layer along the $i = 30$ grid line near the body surface for case A.1 at two values of $\epsilon$.

in the same figure. The figure shows that the wavelength of the second harmonic is approximately half of that of the fundamental mode.

Figure 27 shows the scaled Fourier amplitude $|T'|/\epsilon$ along a parallel grid line near the body surface for two values of $\epsilon$ at $F = 2655$. The fundamental mode ($n = 1$), the second harmonic ($n = 2$), and the mean flow distortion ($n = 0$) for the two cases are plotted in the figure. The scaled amplitudes of the two cases should be the same for linear modes. The receptivity of the fundamental modes is indeed governed by a linear mechanism, while the second harmonic and the mean flow distortion are nonlinear with respect to $\epsilon$.

### 5.5. *Characterization of hypersonic leading-edge receptivity*

The purpose of a receptivity study is to study the link between the induced free boundary-layer waves and the free-stream forcing waves. For an incompressible boundary layer over a flat plate, a receptivity coefficient is defined as the ratio of the induced T–S wave amplitude at the Branch I neutral stability point to the free-stream wave amplitude. In a numerical study of the leading-edge receptivity process, the unsteady solution of the forced response of the boundary layer contains both the Stokes-wave solution and the T–S wave. For incompressible flow, the T–S wave is usually weaker than the Stokes-wave solution. It is necessary to separate the two solutions in order to calculate the receptivity coefficient. Several methods can be used for the decomposition. For example, an incompressible T–S wave solution can be separated from the Stokes-wave solution by recognizing that the Stokes wavelength is an order of magnitude longer than that of the T–S wave (Buter & Reed 1994). Another method (Haddad & Corke 1998) is to compute a corresponding Stokes-wave solution independently by solving a Stokes-wave equation. The T–S wave solution is then obtained by subtracting the Stokes solution from the full Navier–Stokes solution.

These methods for incompressible flow, however, cannot be extended to the current receptivity problem of a hypersonic boundary layer over a blunt leading edge. First, the flow field outside the boundary layer is a non-uniform field bounded by the wall and the bow shock. The unsteady flow in this field is very complex because the bow shock interacts with both the forcing wave from the free stream and the reflected waves from the wall. Such interactions produce, behind the shock, a complex mix of all three kinds of waves in the flow field regardless of the nature of the free-stream forcing wave. Consequently, it is not possible to compute a separate Stokes-wave solution corresponding to the receptivity simulation. In addition, the separation of T–S wave and the Stokes wave solutions based on their disparity in wavelength is also not applicable because the wavelength of the forcing waves in the free stream is of the same order as that of the disturbance waves in the boundary layer. Consequently, a receptivity coefficient like that defined in incompressible flow studies cannot be obtained in the current numerical study.

Despite this difficulty in computing the receptivity coefficient, our results indicate that the forced response in the hypersonic boundary layer contains dominantly boundary layer waves (first mode, second mode, etc) in the leading-edge receptivity process at hypersonic flow conditions. The Stokes-wave component in the solution inside the boundary layer is not significant compared with the boundary layer free waves, as shown by a comparison of the wave fields for two unsteady cases: one induced by free-stream waves and the other induced by surface blow-and-suction from a short surface slot near the leading edge. There is no Stokes wave solution in the second case because there is no free-stream forcing wave. Therefore, if the Stokes wave solution of the first case is a significant part of the forced response in
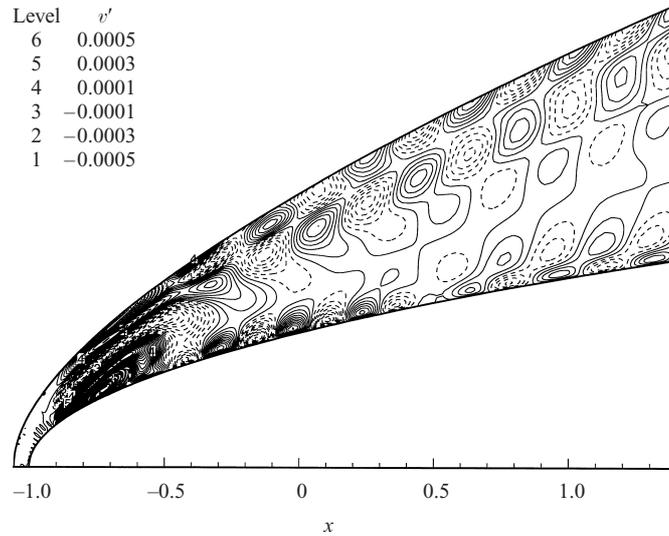
FIGURE 28. Contours of instantaneous perturbations of vertical velocity component ($v'$) after the unsteady solutions reach a time-periodic state for the case of wall blow-and-suction at $F = 2655$.

the boundary layer, the wave structures of the two cases will be very different inside the boundary layer. Otherwise, the Stokes wave solution is not significant and the boundary layer waves are dominant for the current study.

Specifically, we compare the boundary layer wave results of the following two cases: case A.1 of a free-stream acoustic wave at $F = 2655$ and $\epsilon = 5 \times 10^{-4}$, and a case with the same steady base flow but without free-stream disturbances. The unsteady flow of the second case is induced by a surface blowing-and-suction at the same frequency of $F = 2655$ near the leading edge. The wall perturbations are introduced by setting the non-dimensional vertical velocity at the wall to

$$v_{\text{wall}} = \epsilon \sin \left( 2\pi \frac{x - x_0}{x_1 - x_0} \right) \cos \omega t \quad (x_0 \leqslant x \leqslant x_1), \quad (26)$$

where $x_0$ and $x_1$ are the $x$-coordinates of the start and end of the blowing-and-suction strip on the wall. The amplitudes of the wall disturbances are specified by $\epsilon$. In the second case, $x_0 = -0.9$, and $(x_1 - x_0)$ is set to be a half of the free-stream wavelength of case A.1.

Figure 28 shows the contours of instantaneous perturbations of the vertical velocity component ($v'$) after the unsteady solutions reach a time-periodic state for the second case, of wall blowing-and-suction at $F = 2655$. The figure shows the wave field induced by the wall disturbances near the leading edge without free-stream perturbations. The bow shock is perturbed by the acoustic waves originated at the wall. The wave structure inside the boundary layer on the wall show a first and second mode development which is similar to that of case A.1 with free-stream acoustic forcing wave shown in figure 11, though the disturbance wave structures are very different outside the boundary layer.

A quantitative comparison is made by comparing the wave amplitudes of the two cases. Since their absolute amplitudes are different, the relative amplitudes are compared to show that the wave structures inside the boundary layer are very similar
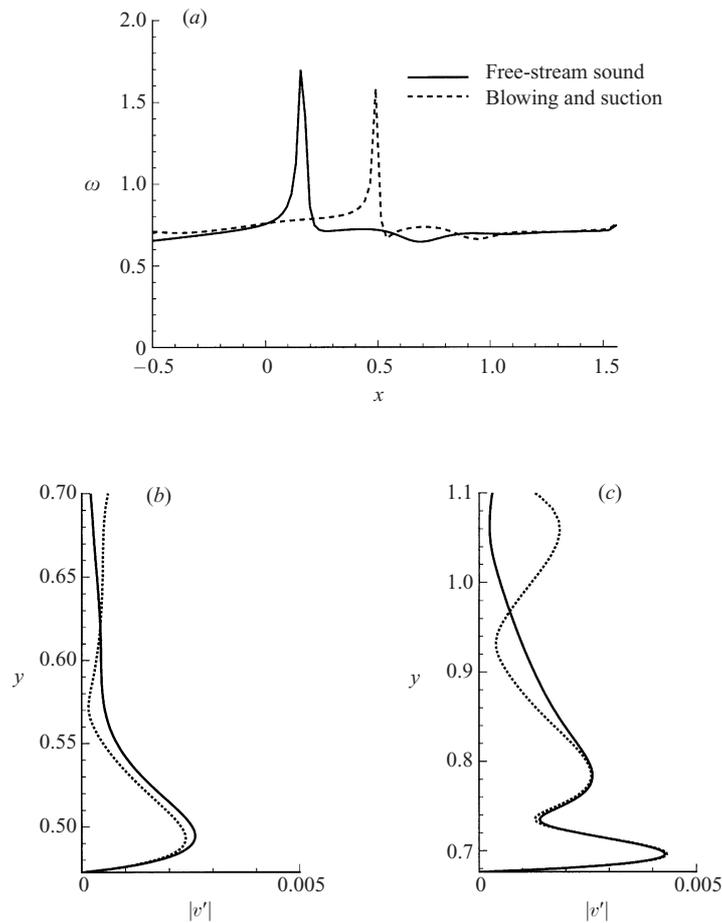
FIGURE 29. Comparison of wave profiles of case A.1 and the case of wall blow-and-suction at the same frequency: (a) normalized vorticity perturbation amplitudes along wall surface; (b) $|v'|$ profile along wall-normal grid line at $x = -0.1066$, (c) $|v'|$ profile along wall-normal grid line at $x = 0.3264$.

for the two cases, which is an indication that the waves induced in the boundary layer in case A.1 have a very weak Stokes wave component.

Figure 29 compares the normalized wave amplitudes of case A.1 and the case of wall blowing-and-suction at the same frequency. The non-dimensional perturbation amplitudes of all flow variables of each case are normalized by the amplitude of local pressure perturbations at the wall. If the disturbances in the boundary layer are dominated by a single T–S type wave, the amplitude profiles of the two cases should be the same, because all wave amplitudes of a single wave change proportionally. If the disturbances contained a mixtures of two or more different waves, the profiles of the two cases will be different. Figure 29(a) compares the normalized vorticity perturbations along the wall for the two cases. The two sets of results agree with each other reasonably well except in the first–second mode transition area. Therefore, the induced waves in the boundary layer are dominantly first mode near the leading edge and second mode afterward. The results are different in the transition area because it contains both first and second mode waves. The locations of wave-mode transition are different for the two cases because of the different forcing mechanisms. Figure 29(b, c)

compares the profiles along two wall-normal grid lines for the normalized vertical velocity perturbations. Near the leading edge (*b*), the agreement is close for the two cases which indicates that the main disturbances are first mode waves, while the difference is due to the Stokes-wave solution in case A.1 and the initial transient solution for the second case. As the flow moves downstream (*c*), the agreement inside the boundary layer becomes very good. These results show that the solutions of the boundary layer responses in the present hypersonic flow conditions are dominated by boundary layer first and higher modes. At the peaks in the first and second mode region, it is expected that the boundary layer responses are mainly first or second mode waves. The Stokes wave solution is very weak. Similar comparisons have also been made for other frequencies, and they lead to the same conclusion.

In addition, comparisons with the LST results also support the conclusion that the response of hypersonic boundary layer at the leading edge has very strong first and higher mode components and has very weak Stokes wave components. One example is the comparison shown in figures 21 and 22 of §5.3. The normalized Navier–Stokes solutions agree very well with single-mode LST results inside the boundary layer. This again shows that the boundary layer response contains mainly boundary layer waves and very little Stokes-wave solutions. The comparison becomes better at further downstream locations or for cases of lower frequencies. The comparison with different types of free-stream disturbances also shows that the wave structures inside the boundary layer are independent of the nature of the forcing waves, which will be shown in figure 33 in §6.1. Again, this is an indication that the waves induced at the leading edge of the wall are dominately boundary-layer first, second, and third modes. The Stokes-wave solution is not significant here.

Based on the results and discussion above, the leading-edge receptivity of a hypersonic boundary layer is approximately characterized in this paper by a new receptivity parameter (instead of the receptivity coefficient) defined as the ratio of maximum disturbance amplitudes in the first mode or second mode regions to the free-stream forcing wave amplitude, i.e.

$$|A| = \frac{|q'|_{max}}{M_\infty \epsilon}, \tag{27}$$

where $|q'|_{max}$ is the Fourier amplitude for a flow variable $q$ at the location of the maximum first or second mode amplitudes in the boundary layer. The free-stream wave amplitude is measured by $M_\infty \epsilon$: it is not exactly the receptivity coefficient, but can serve as an approximate measure of the receptivity strength because the forced response of the boundary layer contains mainly the boundary layer waves in a leading edge receptivity process at hypersonic flow conditions. Therefore, the receptivity parameter $|A|$ defined above is used in this paper.

### 5.6. *Nose bluntness and frequency effects*

The nose bluntness in a study of hypersonic boundary layer receptivity can be characterized by a non-dimensional Strouhal number defined by (14) in which an increase of forcing frequency at a fixed nose radius is equivalent to the increase of relative nose bluntness. The effects of nose bluntness and forcing frequencies on the receptivity of a hypersonic boundary layer is investigated in this paper by considering seven test cases of different forcing frequencies $F$ while holding all other flow parameters fixed. The non-dimensional frequencies of the seven cases are in the range of $F = 531$ to $2655$ corresponding to the Strouhal numbers in the range of $S = 0.4$ to $2$.

| Level | T |
|-------|-------|
| 7 | 0.198 |
| 6 | 0.165 |
| 5 | 0.132 |
| 4 | 0.099 |
| 3 | 0.066 |
| 2 | 0.033 |
| 1 | 0 |

−1.0    −0.5    0    0.5    1.0

| Level | T |
|-------|-------|
| 7 | 0.288 |
| 6 | 0.24 |
| 5 | 0.192 |
| 4 | 0.144 |
| 3 | 0.096 |
| 2 | 0.048 |
| 1 | 0 |

−1.0    −0.5    0    0.5    1.0

| Level | T |
|-------|-------|
| 7 | 0.234 |
| 6 | 0.195 |
| 5 | 0.156 |
| 4 | 0.117 |
| 3 | 0.078 |
| 2 | 0.039 |
| 1 | 0 |

−1.0    −0.5    0    0.5    1.0

$x$
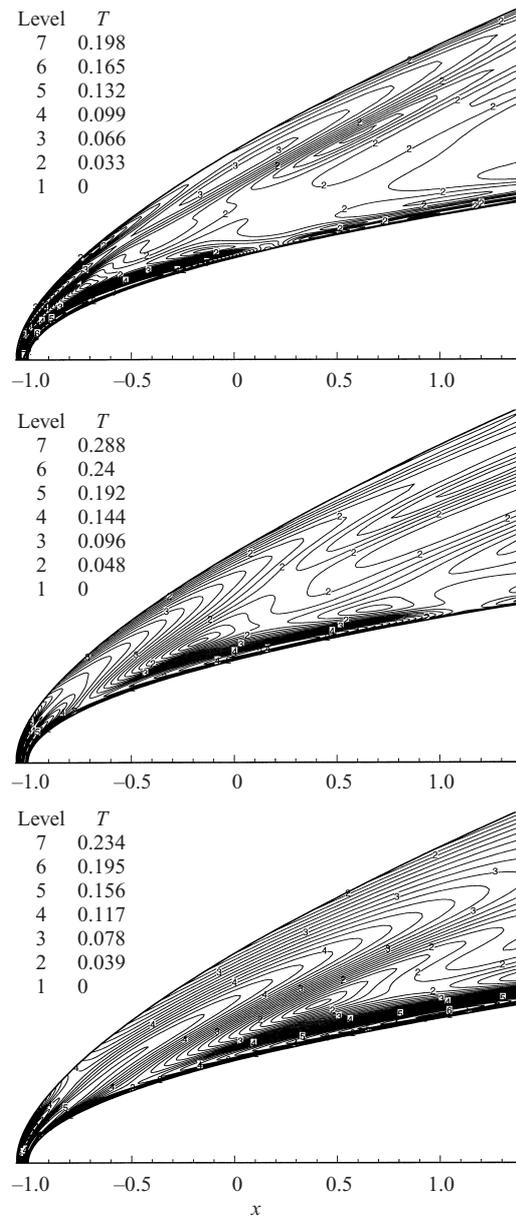
FIGURE 30. Contours of perturbation amplitudes of temperature for three free stream frequencies (from top to bottom: case A.1 $F = 2655$, A.3 $F = 1770$, and A.4 $F = 1327$).

Figure 30 shows the contours of Fourier amplitudes for temperature perturbations for three free-stream forcing frequencies. As the Strouhal number (and frequency) decreases, the region of first mode waves on the wall induced by the receptivity process becomes stronger in amplitude. Meanwhile, the location of maximum of the first mode moves in the downstream direction and the region of first mode growth and decay becomes longer. The contours show that the first mode region is very close to the bow shock for $F = 2655$. It is expected that the presence of the bow shock affects the first mode waves significantly at this frequency. As the frequency decreases,
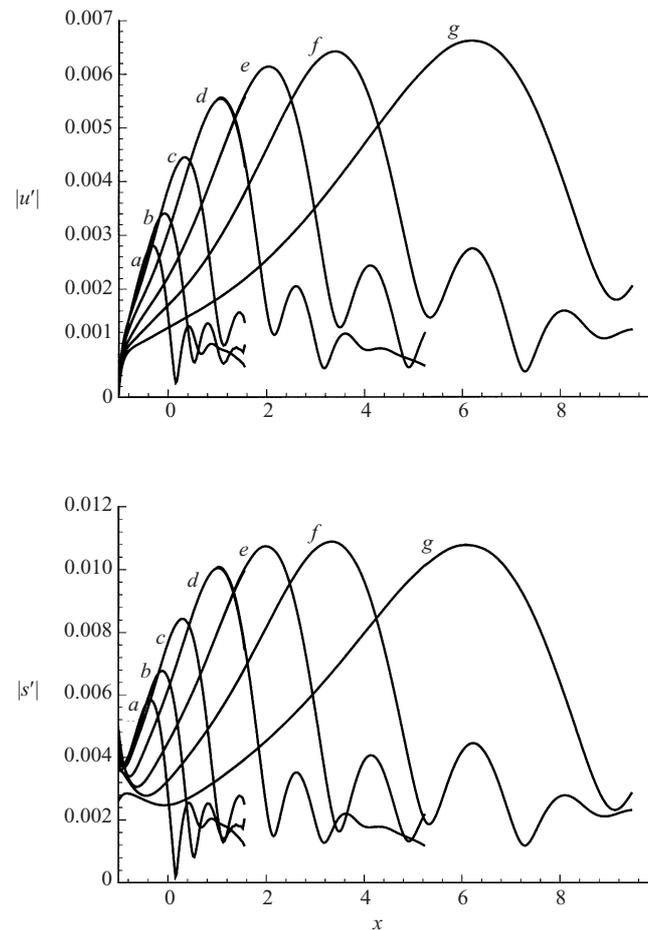
FIGURE 31. Variation of horizontal velocity and entropy perturbation amplitudes along the $i = 30$ grid line near the body surface with seven cases of different forcing frequencies at $\epsilon = 5 \times 10^{-4}$ (cases $a$ to $g$ in the figure correspond to case A.1 to case A.7 respectively).

the first mode region moves downstream, and away from the shock. Therefore the effects of interaction between the shock and the first mode wave decrease as the frequency decreases. The figure also shows that the peak of the first mode wave strength increases as the frequency decreases. This is equivalent to the decrease of wave amplitude in the boundary layer when the relative nose radius increases. This trend can be demonstrated more clearly by the development of wave amplitudes in the boundary layer along the body surface.

Figure 31 shows the distribution of Fourier amplitudes of the fundamental frequency for horizontal velocity and entropy perturbations along a grid line near the body surface for the seven test cases of different frequencies. The results show similar receptivity wave patterns for all frequencies: the first modes grow and decay, followed by the growth and decay of second and third modes respectively. Consistent with linear stability theory results, the second modes have much narrower ranges than do the first modes. As frequency decreases, the maximum first mode amplitudes become larger, their locations move downstream, and the first mode regions extend over much longer ranges. For the present cases, the maximum first mode amplitude reaches a
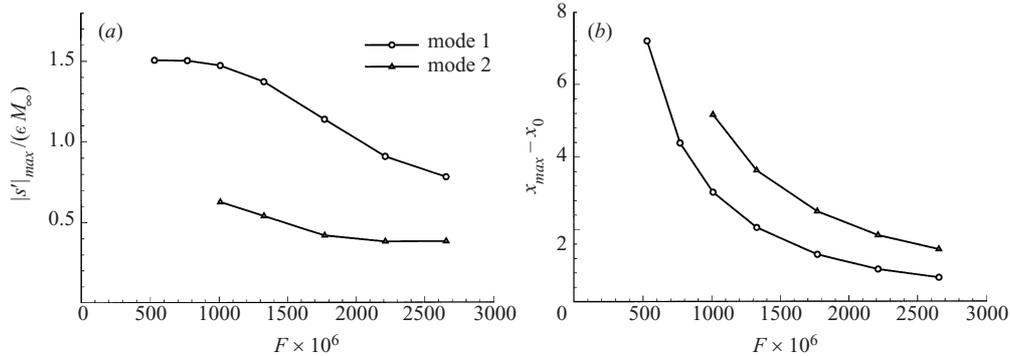
FIGURE 32. (a) Variation of receptivity parameters $|A|$ based on first and second mode amplitudes and (b) locations of maximum amplitudes as a function of forcing frequencies for case A of free stream acoustic waves with $\epsilon = 5 \times 10^{-4}$.

peak value at a non-dimensional frequency around $F = 500$ to $600$. The second mode regions appear further downstream than the first mode regions with higher local Reynolds numbers. Similar to the first mode cases, the second modes increase in strength as frequencies decrease, though they are much weaker than the first mode waves for the current flow conditions.

Figure 32 shows the variation of receptivity parameter $|A|$ defined by entropy perturbations as a function of the frequency. The receptivity parameters calculated based on both the maximum first and second mode amplitudes are plotted in the same figure for comparison. As the frequency decreases, the receptivity parameters for the first modes increase, and approach peak values. The figure also shows that the first mode amplitudes are higher than those of the second modes. The location of the maximum first and second mode amplitudes as a function of frequency is also shown in figure 32. As the frequency decreases, the locations of both maxima move to the downstream. The frequency increase corresponds to the increase of a Strouhal number and the relative nose radius. Therefore, the increase of nose bluntness leads to a decrease in the receptivity parameter in general. At very low frequencies or very low nose bluntness, figure 32 shows that the receptivity parameters are not very sensitive to the change in frequency.

## 6. Parametric studies on receptivity

In the previous section, the receptivity to free-stream fast acoustic waves has been studied in detail. In this section, six additional groups of computational cases are considered to study the effects of different free-stream forcing waves, frequencies, nose bluntness, Reynolds numbers, Mach numbers, and wall cooling on hypersonic receptivity characteristics. The flow conditions of all seven computational cases (case A to case G) are tabulated in Appendix A.

### 6.1. *Effects of different free-stream waves*

For hypersonic flow over a blunt leading edge, the bow shock plays an important role in the leading-edge receptivity process. Before entering the boundary layer, a free-stream disturbance wave will interact with the bow shock first. The interaction of any kind of disturbances with a shock wave will produce four kinds of waves: fast and slow acoustic, entropy and vorticity waves. It is these disturbances generated

| Incident waves | $|p_2'|/(\epsilon M_\infty \gamma p_2)$ | $|s_2'|/(\epsilon M_\infty)$ | $|v_2'|/\epsilon$ |
|---|---|---|---|
| Fast acoustic wave | 0.4716 | 0.5124 | 0 |
| Entropy wave | 0.4023 | 0.6100 | 0 |
| Slow acoustic wave | 0.3423 | 0.6376 | 0 |
| Vorticity wave | 0 | 0 | 1 |

TABLE 1. Linear generation coefficients across a normal shock by free-stream waves
($M_\infty = 15$, $\gamma = 1.4$)

behind the bow shock which propagate or convect downstream to enter the boundary layer. The interaction between free-stream waves and the bow shock produces a complex wave pattern behind the shock because the local shock angle and shock wave strength are different at different locations of the shock. Consequently, the strength of the waves generated and the direction of their wave fronts behind the shock vary along the bow shock. Particularly, the bow shock along the stagnation streamline is a locally normal shock and is strongest. The interaction of a weak free-stream disturbance wave with a planar shock can be predicted by linear theory such as that of McKenzie & Westphal (1968).

Table 1 shows a comparison of pressure, entropy, and vorticity (represented by $|v_2'|$) perturbation amplitudes behind a normal shock generated by the four kinds of incident waves in the free stream for a Mach 15 flow at $\gamma = 1.4$. The strength of free-stream acoustic, entropy, and vorticity waves is measured by $|p_\infty'|/\gamma$, $|s_\infty'|$, and $|v_\infty'|M_\infty$ respectively. They are equal to $\epsilon M_\infty$ in this paper. The table shows that the free-stream fast acoustic waves generate the strongest acoustic wave components behind a normal shock, while the free-stream vorticity waves generate no acoustic waves behind the shock. Specifically, the acoustic wave components generated by free-stream fast acoustic waves are 17% and 38% stronger than those generated by free-stream entropy and slow acoustic waves of the same strength respectively. On the other hand, the entropy wave components generated by free-stream fast acoustic waves are 19% and 24% weaker than those generated by free-stream entropy and slow acoustic waves of the same strength. The vorticity waves do not generate any pressure and entropy perturbations behind a normal shock. Therefore, free-stream vorticity, slow acoustic, entropy and fast acoustic waves represent increasingly stronger acoustic waves behind the shock. A comparison of the receptivity results among the four different kinds of waves in the free stream will show the relative importance of the acoustic and entropy perturbations in generating disturbance waves in the boundary layers.

*Free-stream entropy waves*

The receptivity of hypersonic boundary layers to single-frequency planar entropy waves in the free stream is compared with case A of free-stream fast acoustic waves of the same frequency and free-stream wave amplitude. The flow conditions for the entropy wave cases are listed in the Appendix A as cases B.1 to B.8 for different frequencies. They share the same steady two-dimensional base flow of Mach 15 and Reynolds number 6026.6 over a parabola.

A comparison is made of the contours of instantaneous perturbations of horizontal velocity components for case B.1 free-stream entropy waves and case A.1 acoustic waves of the same frequency at $F = 2655$. It is found that though the wave composition generated at the bow shock by the two forcing waves is different, the wave
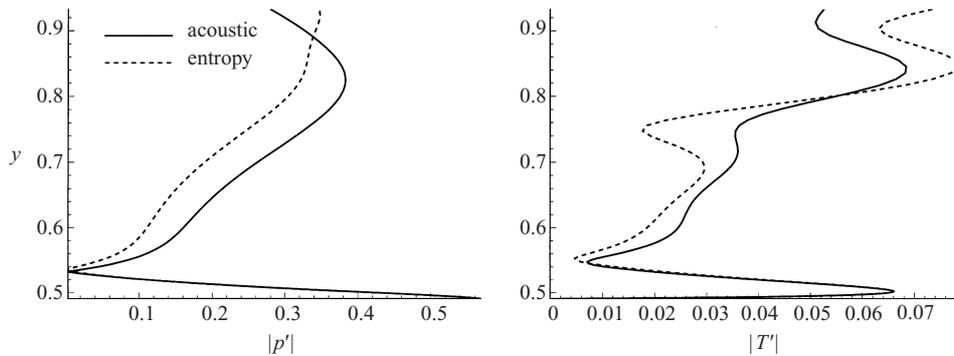
FIGURE 33. Profiles of pressure and temperature amplitudes along the $i = 100$ grid line normal to the parabola surface for two free-stream waves with $F = 2655$ and $\epsilon = 5 \times 10^{-4}$ (acoustic: case A.1, entropy: case B.1).
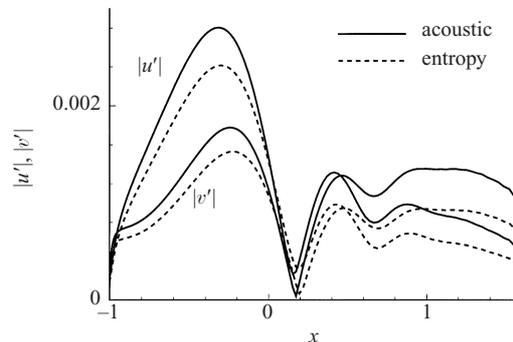


FIGURE 34. Distribution of the Fourier amplitudes of the horizontal velocity perturbations along the $j = 30$ grid line near the parabola surface for two free-stream waves at $F = 2655$ and $\epsilon = 5 \times 10^{-4}$ (acoustic: case A.1, entropy: case B.1).

patterns inside the boundary layer are very similar. Though the wave field outside the boundary layer is very different for the two cases, the two free-stream waves induce the same kinds of boundary layer waves when the frequency of the perturbations is the same. Figure 33 compares the pressure and temperature amplitude profiles along a wall-normal grid line in the first mode wave zone for the two cases of free-stream acoustic and entropy waves of the same frequency. The magnitudes of the induced waves in the boundary layer are different in response to different free-stream forcing waves. But their relative profiles inside the boundary layer should be the same for the same wave mode. In order to compare the two cases, the wave amplitudes of each in the figure are normalized by their respective peak values on or near the wall. The amplitude values of $|p'|$ and $|T'|$ marked on the $x$-axes in the figure are those of case A.1. The figure shows that while the wave amplitude profiles are very different outside the boundary layers (corresponding to $y > 0.54$ in the figure), the induced wave modes at the wall are identical for the two cases. They are the same first mode waves discussed in § 5.

Though the wave form in the boundary layer is the same, the amplitudes of the waves induced in the boundary layer are different for different free-stream forcing waves. Figure 34 compares the distribution of the Fourier amplitudes of $|u'|$ and $|v'|$ along a grid line near the parabola surface for the two cases of free-stream acoustic
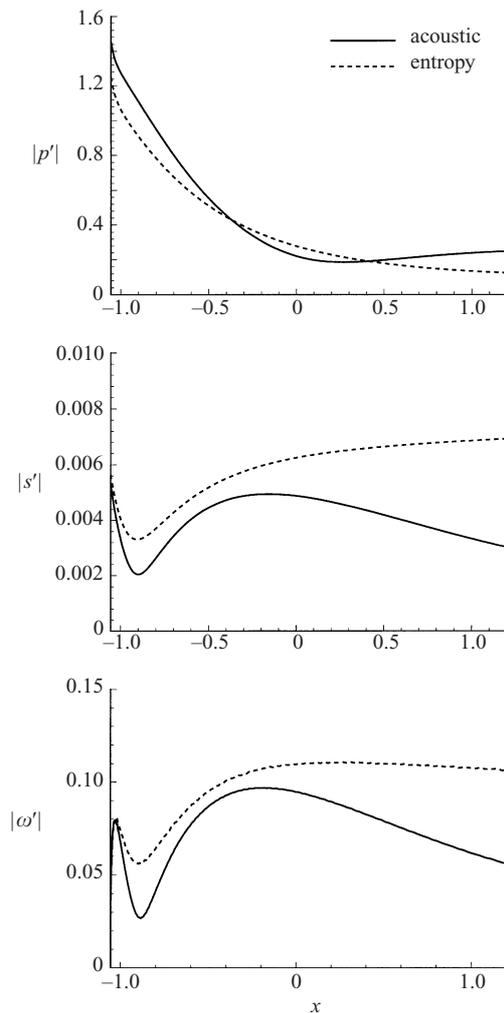
FIGURE 35. Distribution of the Fourier amplitudes of the pressure, entropy, and vorticity perturbations immediately behind the bow shock for two free-stream waves at $F = 2655$ and $\epsilon = 5 \times 10^{-4}$ (acoustic: case A.1, entropy: case B.1).

and entropy waves of the same frequency. Both the first and second modes reach their respective peak values at about the same locations for the two cases. The free-stream acoustic wave generates stronger first and second wave modes in the boundary layer than the free-stream entropy wave does. This is a result of the fact that a free-stream acoustic wave generates a stronger acoustic wave, but weaker entropy and vorticity waves behind the bow shock as shown in table 1. The disturbance waves in the boundary layer are mainly induced by the acoustic waves behind the bow shock. Figure 35 compares the distribution of wave amplitudes of pressure, entropy, and vorticity perturbations immediately behind the bow shock for the two cases. These wave amplitudes represent the strengths of acoustic, entropy and vorticity waves immediately behind the bow shock. They are generated by the combined interaction with the shock by the free-stream forcing waves and the reflected acoustic waves behind the shock. This figure shows that the free-stream entropy waves generate
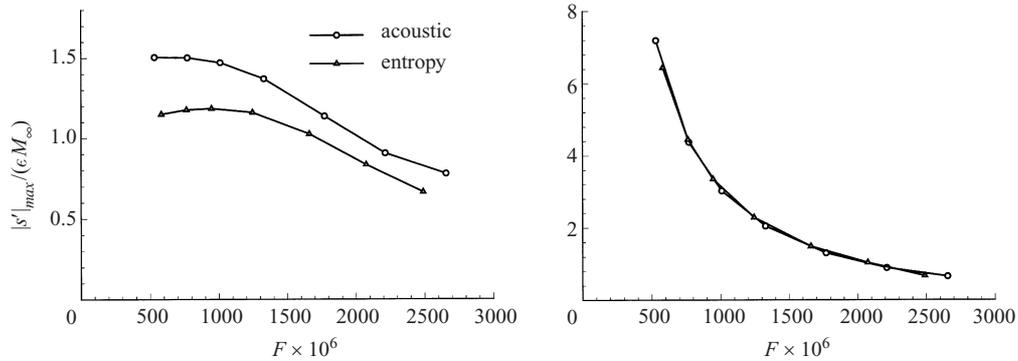
FIGURE 36. Comparison of amplitudes of receptivity parameter $|A|$ and location of maximum amplitude as a function of $F$ between two free-stream fast acoustic and entropy waves with $\epsilon = 5 \times 10^{-4}$ (acoustic: case A; entropy: case B).

stronger entropy and vorticity perturbations behind the shock but weaker pressure perturbations near the leading edge. The weaker acoustic waves behind the bow shock generated by the free-stream entropy wave leads to weaker first and second mode waves in the boundary layer. As shown later in this paper, the same trend is observed for all other free-stream waves. Therefore, these results and similar results for other cases presented in this paper show that the acoustic wave is mainly responsible for penetrating the boundary layer to generate boundary-layer waves. The entropy and vorticity waves generated at the bow shock do not have a strong interaction with the boundary layer.

The effects of frequency and nose bluntness on the receptivity process for case B of free-stream entropy waves are investigated by the numerical simulation of several cases at different frequencies. The results show the same wave patterns in the boundary layer as those of the free-stream acoustic waves shown in §5. Figure 36 compares the receptivity parameters induced by free-stream fast acoustic and entropy waves as a function of non-dimensional frequency $F$, which is proportional to the Strouhal number. The receptivity parameter in the figure is evaluated based on maximum entropy perturbations in the first mode region. Results for $|A|$ based velocity perturbations are also found to follow a very similar trend. The corresponding comparison of the location of maximum entropy amplitude between the two cases is also shown in figure 36. The receptivity parameters of free-stream entropy waves are weaker than those of free-stream acoustic waves, but the locations of maximum wave amplitudes are the same. The maximum receptivity parameters are approximately 1.2 and 1.5 for fast acoustic and entropy waves respectively. The difference is due to the fact that the free-stream fast acoustic waves generate 17% stronger acoustic wave components behind the normal bow shock than do the free-stream entropy waves. The corresponding difference in the receptivity parameters is roughly of the same order of magnitude.

Figure 36 also shows the effects of nose bluntness or frequency on the receptivity parameters for the two cases. For both the free-stream acoustic and entropy waves, as the frequency $F$ decreases, the receptivity parameter increases and approaches a peak value as $F$ is further reduced. Since $F$ is proportional to Strouhal number $S$, as the relative nose radius decreases, the receptivity parameter will in general increase, but reach a maximum if the nose radius further decreases. This trend is the same
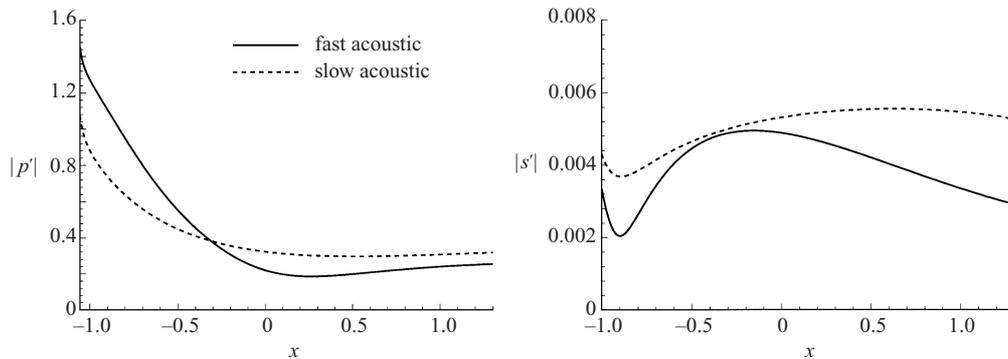
FIGURE 37. Distribution of the Fourier amplitudes of the pressure and entropy perturbations immediately behind the bow shock for free-stream fast and slow acoustic waves at $F = 2655$ and $\epsilon = 5 \times 10^{-4}$ (fast acoustic: case A.1, slow acoustic: case C.1).

for both cases. For the free-stream entropy waves, the receptivity parameters slightly decrease when frequency $F$ is lower than 500.

*Free-stream slow acoustic waves*

The receptivity of hypersonic boundary layers to single-frequency planar slow acoustic waves in the free stream is compared with that of case A of free-stream fast acoustic waves. The flow conditions of the slow acoustic wave cases are listed in Appendix A as cases C.1 to C.7 for different $F$ ranging from 531 to 2655.

Similar to the preceding cases of free-stream entropy waves, it is found that the disturbance waves induced by the free-stream slow acoustic waves are the same as those induced by other waves. Different kinds of free-stream forcing waves induce different amplitudes of the same disturbance waves in the boundary layer. The acoustic waves are mainly responsible for the generation of disturbance waves in hypersonic boundary layers. As shown in table 1, slow acoustic waves in the free stream generate 38% weaker acoustic wave components behind a normal shock than do fast acoustic waves. The distributions of wave amplitudes for pressure and entropy perturbations immediately behind the bow shock for the two cases of free-stream fast and slow acoustic waves of the same frequency are compared in figure 37. The slow waves generate stronger entropy perturbations behind the shock but much weaker pressure perturbations near the leading edge. The weaker acoustic waves behind the bow shock in the free stream generate much weaker induced waves in the boundary layer. This confirms again the observation stated earlier that the acoustic waves behind the bow shock are mainly responsible for penetrating the boundary layer to generate disturbance waves.

Seven cases of free-stream slow acoustic waves with different frequencies are computed to study the effect of Strouhal numbers and frequencies on the receptivity amplitudes. Figure 38 compares the receptivity parameter $|A|$ induced by free-stream fast and slow acoustic waves as a function of non-dimensional frequency $F$. It is found that the corresponding location of maximum entropy amplitude for free-stream fast waves is the same as for the slow acoustic waves. The receptivity parameters for free-stream slow acoustic waves is much weaker than those for the fast acoustic waves and entropy waves (see figure 36), but the location of maximum wave amplitude is almost the same for all three kinds of free-stream waves, with those for the slow acoustic waves being slightly larger.
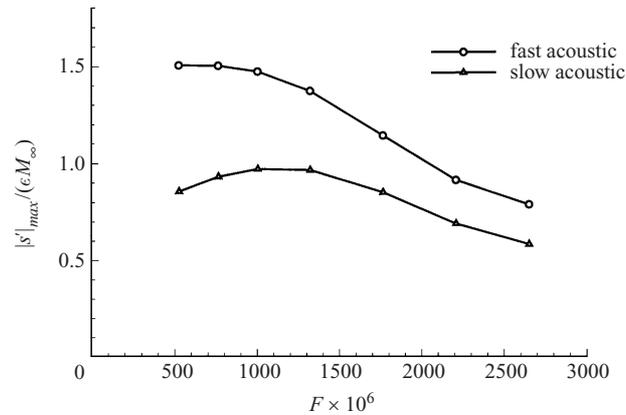
FIGURE 38. Distribution of receptivity parameter $|A|$ vs. frequency $F$ for two free-stream fast and slow acoustic waves at $\epsilon = 5 \times 10^{-4}$ (fast acoustic: case A, slow acoustic: case C).

The effects of frequency or nose bluntness on the receptivity parameters are also shown in figure 38 since the Strouhal number $S$ is proportional to frequency $F$. For both free-stream fast and slow acoustic waves, as the frequency decreases, the receptivity parameters for the first modes increase, and approach a peak value as $F$ is further reduced. Then, for $F$ still lower, the receptivity parameter trend for the case of slow acoustic waves will reverse and become slightly lower than the peak value. Therefore, as the nose radius decreases, the receptivity parameter will in general increase, reach a peak value, and then slightly decrease.

*Free-stream vorticity waves*

The receptivity of hypersonic boundary layers to planar vorticity waves in the free stream is compared with that of case A of free-stream fast acoustic waves. The flow conditions of the free-stream vorticity waves are listed in the Appendix 1 as cases D.1 to D.7 of different frequencies $F$ ranging from 531 to 2655. The free-stream vorticity waves generate no acoustic waves behind a normal bow shock (see table 1). The main wave components generated by the free-stream vorticity waves behind the bow shock are vorticity waves. Since it is found that the generation of boundary layer waves is mainly a result of the acoustic wave interaction with the boundary layer, it is expected that the receptivity parameters of case D will be much smaller than those of case A of free-stream fast acoustic waves.

Table 1 shows that a vorticity wave in the free stream generates no pressure perturbations behind a normal bow shock. The actual distributions of wave amplitudes for pressure and vorticity perturbations immediately behind the bow shock for free-stream fast and slow acoustic waves of the same frequency are shown in figure 39. The free-stream vorticity waves generate much weaker acoustic wave components behind the bow shock. They generate a stronger vorticity at the shock only in a very narrow region near the stagnation centreline. The weak acoustic wave behind the bow shock for free-stream vorticity wave generates weak first and second mode waves in the boundary layer. Therefore, free-stream vorticity waves are the most ineffective in penetrating the boundary layer to generate disturbance waves because they generate the weakest acoustic wave at the bow shock among all four kinds of forcing waves.

A number of cases of receptivity to free-stream vorticity waves of different fre-
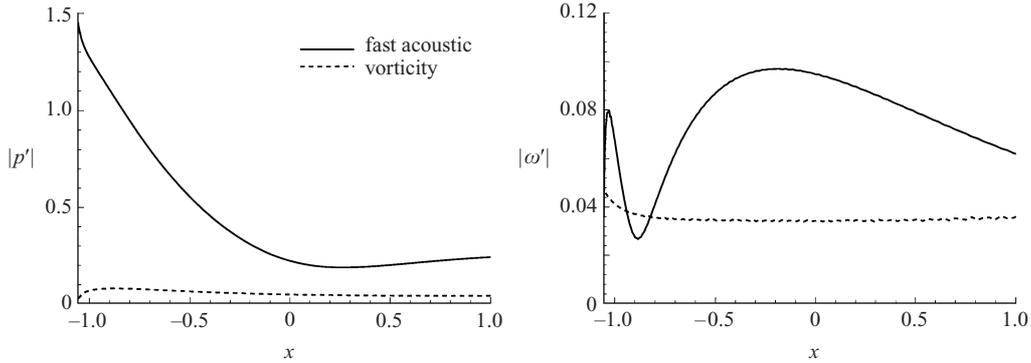
FIGURE 39. Distribution of the Fourier amplitudes of the pressure and vorticity perturbations immediately behind the bow shock for a free-stream fast acoustic wave and vorticity wave at $F = 2655$ and $\epsilon = 5 \times 10^{-4}$ (fast acoustic: case A.1, vorticity: case D.1).
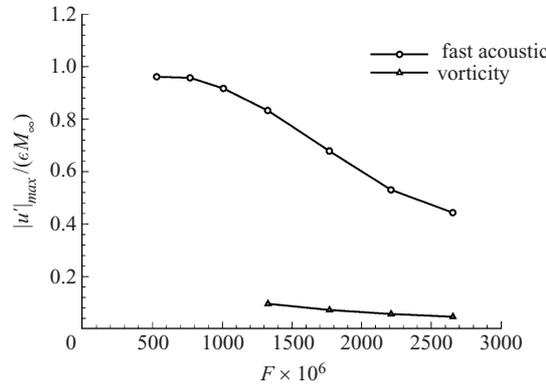


FIGURE 40. Distribution of receptivity parameter $|A|$ vs. frequency $F$ for free-stream fast acoustic and vorticity waves at $\epsilon = 5 \times 10^{-4}$ (fast acoustic: case A, vorticity: case D).

quencies has been computed to study the effect of Strouhal numbers and frequencies on the receptivity process. Figure 40 compares the variation of receptivity parameter $|A|$ induced by free-stream fast acoustic waves and vorticity waves as a function of non-dimensional frequency $F$. The receptivity parameter in this figure is evaluated based on the results of horizontal velocity perturbations. The receptivity parameters for free-stream vorticity waves are an order of magnitude weaker than those for the fast acoustic waves. They are also much weaker than those for the slow acoustic waves and entropy waves (figures 36 and 38). The figure also shows that, for both kinds of free-stream waves, as the frequency decreases, the receptivity parameter for the first mode increases and approaches a peak value as $F$ is further reduced. Therefore, as the relative nose radius decreases, the receptivity parameters will in general increase. It is also found that, similar to cases A, B, and C, the wave modes induced in the boundary layer are independent of the nature of free-stream waves.

### 6.2. *Reynolds number effects*

The Reynolds number effects on the receptivity process are studied by the numerical simulations of the receptivity to free-stream fast acoustic waves at two Reynolds
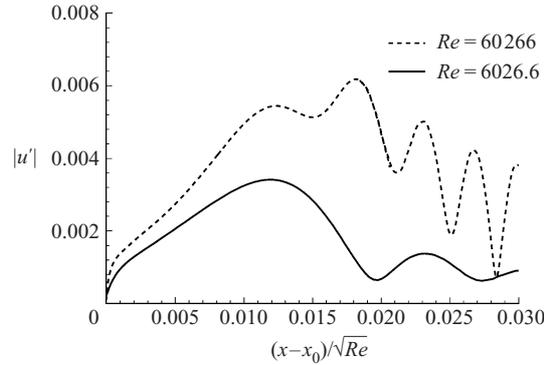
FIGURE 41. Comparison of the Fourier amplitudes of the horizontal velocity perturbations along the $j = 30$ grid line near the parabola surface for two cases of free-stream fast acoustic waves at $S = 1.67$ and $\epsilon = 5 \times 10^{-4}$ but with different Reynolds numbers ($Re = 6026.6$: case A.2, $Re = 60\,266$: case E.2).

numbers. Listed in Appendix A are the flow conditions for the case E of higher Reynolds number with $F$ ranging from 101 to 266 corresponding to $S$ in the range of 0.76 to 2.43. Case E has the same flow conditions as case A except that the Reynolds number is made 10 times as large by increasing the size of the parabola by 10 times. The results of case A and case E with the same Strouhal number are compared to investigate the Reynolds number effects on the receptivity process. Unlike cases A to D, the steady base flow solutions of case E are different from those of case A.

The first case of higher Reynolds numbers has the following flow conditions: $\epsilon = 5 \times 10^{-4}$, $F = 265.5$, and a Strouhal number of $S = 2$. The computational results show that for cases A and E with the same Strouhal number, the location where the first mode wave reaches its maximum amplitude is approximately proportional to $\sqrt{Re_\infty}$. This is shown by figure 41 which compares the Fourier amplitudes of the horizontal velocity perturbations along a grid line near the parabola surface. The $x$-axis is normalized by $\sqrt{Re_\infty}$ for comparison. The figure clearly shows that the first modes reach their maximum at about the same value of $x_{max}/\sqrt{Re_\infty}$ for the two different Reynolds numbers. All other Strouhal numbers also show the same result that $x_{max}/\sqrt{Re_\infty}$ is the same for different Reynolds numbers but with the same Strouhal number. On the other hand, the locations where the second modes reach their maximum amplitudes do not follow the same trend. The figure also shows much stronger receptivity parameters for the case of higher Reynolds number. Contrary to case A.2 with a lower Reynolds number, the second mode of the higher Reynolds number case is stronger than the first mode wave amplitudes, which indicates that the second mode becomes more unstable at higher Reynolds numbers.

The effects of Strouhal numbers or the relative nose bluntness on the receptivity parameters for case E are compared with those of case A of lower Reynolds number. Figure 42 compares the receptivity parameter $|A|$ induced by free-stream fast acoustic waves as a function of the Strouhal number for the two Reynolds numbers. The figure shows that the receptivity parameters for case E of higher Reynolds number are much larger than those for case A. Both Reynolds numbers show the same trend that the receptivity becomes stronger when the Strouhal number or the nose bluntness decreases. Figure 42 also shows the locations of maximum first-mode amplitudes defined by $x_{max}/\sqrt{Re_\infty}$ vs. Strouhal numbers for the two free-stream
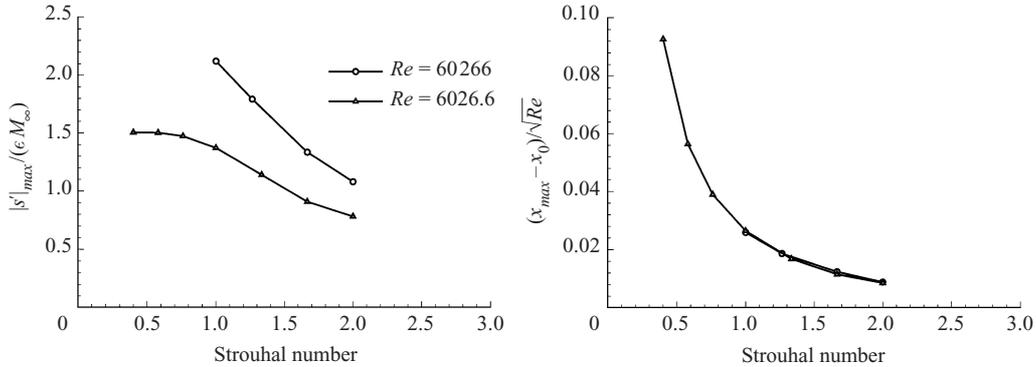
FIGURE 42. Distribution of receptivity parameter $|A|$ and location of maximum first-mode amplitudes normalized by the square root of Reynolds numbers as a function of Strouhal number $(\omega^* r^*/U_\infty^*)$ for two groups of cases of different free-stream Reynolds numbers at $\epsilon = 5 \times 10^{-4}$ ($Re = 6026.6$: case A, $Re = 60\,266$: case E).
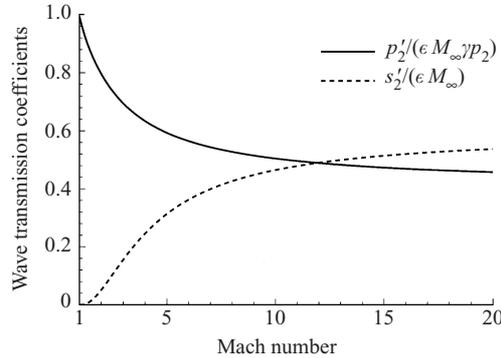


FIGURE 43. Linear transmission coefficients for pressure and entropy perturbations as a function of free-stream Mach number, due to the interaction of free-stream fast acoustic waves with a normal shock ($\gamma = 1.4$).

Reynolds numbers. The figure confirms the observation that for the frequencies computed, the locations of maximum first-mode wave amplitudes are very similar for the two cases when the distances from the leading edge are normalized by $\sqrt{Re_\infty}$.

### 6.3. *Compressibility effects*

The compressibility effects on the receptivity process are studied by comparing the results of case F for Mach 8 with those of case A for Mach 15, while all other non-dimensional parameters, $Re_\infty$, $\gamma$, $Pr$, and $T_w/T_0$, are held constant. Listed in Appendix A are the flow conditions of case F, with frequencies and Strouhal numbers of the free-stream fast acoustic waves in the range of $F = 531$ to $2655$ and $S = 0.2$ to $2$ respectively.

Since the bow shocks of the steady base flows are stronger for higher Mach numbers, the receptivity is affected by the change in Mach number in two respects, (i) by the change of the interaction between the bow shock and free-stream forcing waves, and (ii) by the change of the compressibility of the boundary layer. For the first, the linear transmission of free-stream fast acoustic waves through a normal shock at zero incident angle, the ratio of perturbations before and after the shock can
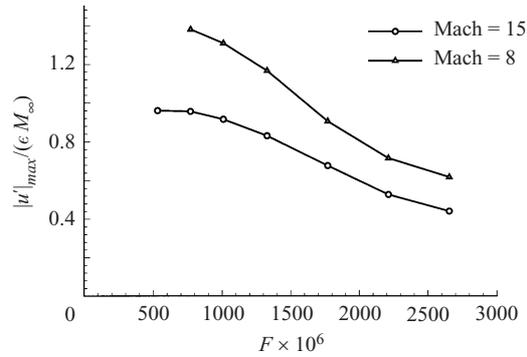
Figure 44. Distribution of receptivity parameter $|A|$ based on horizontal velocity vs. frequency for two free-stream Mach numbers at $\epsilon = 5 \times 10^{-4}$ (Mach = 15: case A; Mach = 8: case F).

be computed by using a linear theory. Figure 43 shows the linear pressure and entropy transmission coefficients as a function of Mach numbers for free-stream fast acoustic waves passing through a normal shock. The transmission coefficient is 1 for pressure and 0 for entropy in the isentropic weak-shock limit of Mach number 1. As the Mach number increases, the fast acoustic wave in the free stream generates a weaker acoustic wave but a stronger entropy wave behind the bow shock. The transmission coefficient approaches constant values for both acoustic and entropy components in the high Mach number limit. For case F with Mach 8, the transmission coefficient for pressure, $|p'_2|/(\epsilon M_\infty \gamma p_2)$, has a value of 0.5265, which is 12% larger than the corresponding value for case A with Mach 15 shown in table 1. On the other hand, $|s'_2|/(\epsilon M_\infty) = 0.4255$, which is 14% smaller than the corresponding value for case A. Therefore, the higher Mach number produces weaker acoustic waves behind the bow shock before entering the boundary layer. The change of the induced waves in the boundary layer for higher Mach number is a result of the combined effect of weaker acoustic waves behind the shock and stronger compressibility in the boundary layer.

The effect of compressibility on the receptivity to free-stream fast acoustic waves is studied by comparing the results of cases A and F with two Mach numbers. The effects of frequencies or Strouhal numbers for the relative nose bluntness on the receptivity parameters are compared for the two Mach numbers. Figure 44 compares the variation of the receptivity parameter $|A|$ induced by free-stream fast acoustic waves as a function of frequency $F$ and shows that the receptivity parameter for case A of higher Mach number is much weaker than the lower Mach number. The difference is larger than the 12% difference in transmission coefficients across the shock. The additional difference is attributed to the change in compressibility in the boundary layers. In other words, the increase of Mach number leads to weaker receptivity parameter due to the combined effects of stronger bow shock and higher compressibility in the boundary layers. On the effects of nose bluntness, both Mach numbers show the same trend in the receptivity parameter: the receptivity becomes weaker when the Strouhal number or the nose bluntness increases. Therefore, the increase of Mach number leads to the reduction of the overall receptivity parameter in the boundary layer, caused by both the decrease in the transmission coefficients for acoustic waves at the bow shock and the reduction in the receptivity in higher Mach number boundary layers.
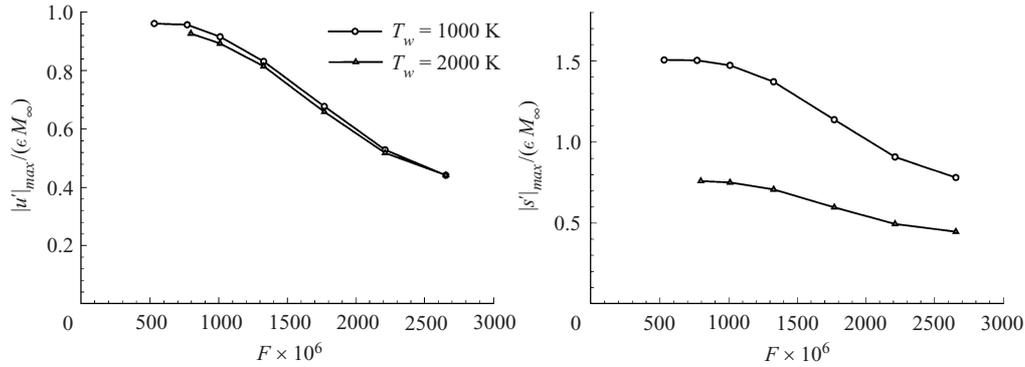
FIGURE 45. Distribution of receptivity parameter $|A|$ based on horizontal velocity and entropy vs. frequency for two wall temperatures at $\epsilon = 5 \times 10^{-4}$ ($T_w^* = 1000$ K: case A; $T_w^* = 2000$ K: case G).

### 6.4. *Wall cooling effects*

It has been shown using linear stability analysis (Mack 1984) that wall cooling stabilizes the first mode but destabilizes the second mode in a hypersonic boundary layer over a flat plate. This wall-cooling effect is valid for the linear growth or decay of boundary-layer wave modes after they are generated in the boundary layer by a receptivity process. On the other hand, the wall cooling effect may be different for the initial receptivity process because it is governed by a different mechanism. In this section, the wall-cooling effect on the hypersonic leading-edge receptivity is studied by comparing the acoustic receptivity for cases A and G of different wall temperatures. Both cases have relatively cold walls with respect to the free-stream total temperature. The wall to free-stream total temperature ratios are $T_w/T_0 = 0.1126$ and $0.2253$ for cases A and G respectively. All other non-dimensional parameters of the two cases, $M_\infty$, $Re_\infty$, $\gamma$, and $Pr$ are the same. The free-stream forcing waves of case G are fast acoustic waves of frequency ranging from 797 to 2655 corresponding to the Strouhal numbers $S$ in the range 0.6 to 2.

Figure 45 compares the variation of receptivity parameter $|A|$ induced by free-stream fast acoustic waves for the two wall temperatures and shows that the wall cooling results in slightly stronger velocity perturbations and much stronger entropy perturbations in the boundary layer. The reason for the larger difference in the entropy perturbations is that the steady base flows of the two cases have very different temperature profiles near the wall. The entropy perturbations are affected strongly by the change of wall temperatures of the base flows. Therefore, the velocity perturbations are a more accurate measurement of the relative strength of waves induced in the boundary layer. This figure shows that the effect of wall cooling on the receptivity amplitudes is opposite to the wall cooling effect on linear growth or decay of wave modes in the boundary layer. Meanwhile, the results also show that the locations of the peak in the first mode and the second mode are not very sensitive to the changes in wall temperatures. The locations of maximum amplitudes moves slightly downstream when the wall temperature is lower.

## 7. Summary and discussion

The receptivity of a hypersonic boundary layer to free-stream disturbances for a two-dimensional Mach 15 flow over a parabola has been studied by numerical simu-

lations. The study is based on the solutions of full Navier–Stokes equations obtained by the simulations, while results of approximate analytical analyses are compared with the Navier–Stokes solutions for a better understanding of the numerical results. The main findings of the study are summarized below.

Steady flow solutions are studied in this paper with the focus on the interaction between the inviscid vorticity field generated by the bow shock and the viscous vorticity field in the boundary layer. The numerical Navier–Stokes solutions agree very well with theoretical predictions of vorticity generation by the bow shock and approximate local similarity solutions in the boundary layer. Steady results show that inflectional velocity profiles are always generated at the edge of the boundary layer due to the vorticity interaction. The vorticity interaction is stronger at lower $Re_\infty$, higher $M_\infty$, or smaller $\gamma$.

The unsteady results show that the free-stream acoustic disturbances generate first, second, and third mode waves in the boundary layer on the wall. The first mode waves are always generated near the leading edge and are amplified before decaying rapidly. The second mode waves are the dominant mode after the first mode decay. The first mode waves have very strong vorticity while the second mode waves have relatively weak vorticity. The first, second, and third modes are identified by comparison with eigenfunctions obtained from an independent linear stability analysis. Inside the boundary layer, the waves modes obtained by the numerical simulations agree well with the eigenmodes obtained by the linear stability analysis. The spatial wavenumbers of the simulations also agree reasonably well with the linear stability results. The agreement becomes better for lower frequency where the effect of the bow shock becomes weaker due to the wave modes developing downstream.

It is shown that the waves induced at the leading edge of the wall are dominantly boundary-layer first, second, and third modes. The Stokes-wave solution is not significant for the current case of leading-edge receptivity of high Mach number flows over a blunt body. Based on these results, the leading-edge receptivity of hypersonic boundary layers is approximately characterized in this paper by a new receptivity parameter defined as the ratio of maximum disturbance amplitudes at the first mode or second mode regions to the free-stream forcing wave amplitude.

The nose bluntness is characterized by the Strouhal number which shows that the increase of forcing frequency at a fixed nose radius is equivalent to the increase of relative nose bluntness. The effects of nose bluntness and forcing frequencies on the receptivity of a hypersonic boundary layer are investigated by considering seven test cases of different forcing frequencies while holding all other flow parameters fixed. It is found that as the frequency decreases, the maximum first and second mode amplitudes and the region of the first and second modes increases substantially. The results also show that the receptivity parameter and the region of the first mode increase substantially when the forcing frequency decreases. As the frequency decreases further, the receptivity parameters for the first modes approach peak values. These results indicate that the receptivity parameters increase as the relative nose radius decreases, but there is a critical nose bluntness (or frequency) which corresponds to maximum receptivity parameter.

The nonlinearity of the receptivity process is studied by considering a number computational cases with different free-stream forcing wave amplitudes. The results show that the generation of the first and second mode waves of the fundamental forcing frequency is linear with respect to the weak forcing amplitudes in the free stream. The receptivity also generates nonlinear superharmonics and mean flow distortion.

A parametric study of the leading-edge receptivity of hypersonic boundary layers to free-stream disturbance waves has been carried out on the effects of different free-stream waves, frequencies, nose bluntness, Reynolds numbers, Mach numbers, and wall cooling.

The effects of different free-stream waves on the receptivity process are studied first. For each of the four kinds of waves in the free stream, a number of sub-cases are computed with different non-dimensional frequencies or Strouhal numbers. The results show that for all kinds of forcing waves and all frequencies considered in this paper, the free-stream forcing waves always generate first, second, and high mode waves in the boundary-layer. The first mode is always generated near the leading edge and is amplified before decaying rapidly. The second mode is the dominant mode after the first mode decay. All results show that the generation of disturbance waves in the boundary layer near the blunt leading edge is mainly due to the acoustic waves entering the boundary layers. The entropy and vorticity waves behind the bow shock do not interact very much with the boundary layer because they propagate along the streamlines, which do not intersect with the boundary layer. An indication of this is the fact that for different kinds of free-stream waves, the receptivity parameters are larger for stronger acoustic components behind the bow shock in the leading-edge region. As shown in table 1, the free-stream fast acoustic waves generate the strongest acoustic wave components behind the bow shock with weakest entropy wave components. As a result, they generate the strongest receptivity parameters in the boundary layer. On the other hand, the free-stream vorticity waves generate almost no acoustic wave components behind the bow shock. Their receptivity parameters are an order of magnitude smaller than those of free-stream fast acoustic waves. All these results show that acoustic waves generated at the bow shocks are mainly responsible for generating hypersonic boundary layer instabilities near the leading edge. Entropy and vorticity waves are not effective in the hypersonic boundary receptivity process.

The effects of Reynolds number on the receptivity process for the case of fast acoustic waves have been studied by comparing two Reynolds numbers. The increase in free-stream Reynolds number leads to a substantial increase in the receptivity parameter. As the Reynolds number increases, the second mode becomes much stronger, stronger than the first mode for some cases of lower frequencies. It is also found that the location of the maximum first mode amplitudes is proportional to $\sqrt{Re_\infty}$ for the same free-stream waves of the same Strouhal number. The perturbation wave profiles across the boundary layer are the same for the same Strouhal number but different Reynolds numbers.

The compressibility effects are considered for two Mach numbers of 8 and 15. The difference in Mach number affects both the compressibility in the boundary layer and the transmission coefficients of free-stream waves interacting with the bow shock. It is found that the increase in Mach number reduces the receptivity parameters significantly due to the combined effects of stronger bow shock and higher compressibility in the boundary layer. The increase of Mach number leads to the reduction of the overall receptivity parameter in the boundary layer. The reduction of the receptivity parameters is caused by both the decrease in the transmission coefficients for acoustic waves at the bow shock and the reduction in the receptivity in higher Mach number boundary layers.

The wall-cooling effects on the hypersonic leading edge receptivity are studied by comparing the acoustic receptivity for two wall temperatures. The results show that wall cooling increases the first-mode receptivity parameter or wave perturbations

generated in the boundary layers, though the effects are not very strong for the velocity perturbations. This is different from the results of wall-cooling effects on the linear stability of the first mode in compressible boundary layer, where wall cooling stabilizes the first mode. The difference in the wall-cooling effect is due to the fact that the receptivity is governed by the different mechanism of an initial-boundary value problem.

## Appendix A. Flow conditions of computational cases

Seven groups of computational cases are considered to study parametric effects of nondimensional frequency, nose bluntness (Strouhal number), Reynolds number, Mach number, wall cooling, and different kinds of free-stream waves, on the receptivity of hypersonic flows over parabolic bodies. The flow conditions of the seven groups of computational cases are given in table 2.

## Appendix B. Code validation and numerical accuracy

For the numerical results presented in this paper, much effort has been made to evaluate the correctness and the accuracy of the numerical solutions for both steady and unsteady flow solutions. There are two main aspects of the validations process: (i) to ensure the solutions provide the correct physical solutions by comparing with theoretical solutions and experimental results; (ii) the numerical accuracy of the solutions needs to be assessed by grid refinement studies. Both have been done for many steady and unsteady viscous flow computations. Some of the results have been presented in an earlier paper on the numerical aspects of our studies. Details of those studies can be found in Zhong (1998), they are not repeated here. The grid refinement for numerical results relevant to this paper are briefly discussed below.

The first step is to evaluate the physical correctness of the numerical solutions by comparison with theoretical and experimental results. The two- and three-dimensional fifth-order computer codes for the unsteady full Navier–Stokes equations have been extensively tested and validated for many steady and unsteady flow simulations. The code has been tested for a diverse range of test cases with and without bow shocks for both steady and unsteady flows. Examples of the test cases are hypersonic viscous flow over a circular cylinder, hypersonic viscous flow over a sphere, hypersonic viscous flow over a non-axisymmetric elliptical cone, supersonic Couette flows, supersonic boundary layer flow over a flat plate, and others. Many results have been published in our previous papers.

For the current case, there are no experimental results. The numerical solutions of the Navier–Stokes equations are compared with theoretical results for both viscous and inviscid regions. Some such comparisons are presented in the paper in Figs. 6, 7, 9, 10, 15, 20, 21, and 22. The numerical accuracy of the results is evaluated by a grid refinement study. Both steady and unsteady solutions have been checked on two sets of grids of $161 \times 121$ and $321 \times 241$. Figure 4($c$) shows an example of the grid refinement

| Case # | $k_\infty$ | $F$ | $S$ | Case # | $k_\infty$ | $F$ | $S$ |
|--------|--------|--------|------|--------|--------|--------|------|
| A.1 | 15 | 2655 | 2.00 | A.5 | 5.7 | 1008.9 | 0.76 |
| A.2 | 12.5 | 2212.5 | 1.67 | A.6 | 4.35 | 769.95 | 0.58 |
| A.3 | 10 | 1770 | 1.33 | A.7 | 3 | 531 | 0.40 |
| A.4 | 7.5 | 1327.5 | 1.00 | | | | |
| B.1 | 16 | 2655 | 2.00 | B.5 | 7.5 | 1244.5 | 0.94 |
| B.2 | 15 | 2489.1 | 1.88 | B.6 | 5.7 | 945.84 | 0.71 |
| B.3 | 12.5 | 2074.2 | 1.56 | B.7 | 4.6 | 763.31 | 0.58 |
| B.4 | 10 | 1659.4 | 1.25 | B.8 | 3.5 | 580.78 | 0.44 |
| C.1 | 17.143 | 2655 | 2.00 | C.5 | 6.5143 | 1008.9 | 0.76 |
| C.2 | 14.286 | 2212.5 | 1.67 | C.6 | 4.9414 | 769.95 | 0.58 |
| C.3 | 11.429 | 1770 | 1.33 | C.7 | 3.4286 | 531 | 0.40 |
| C.4 | 8.5714 | 1327.5 | 1.00 | | | | |
| D.1 | 16 | 2655 | 2.00 | D.5 | 6.08 | 1008.9 | 0.76 |
| D.2 | 13.333 | 2212.5 | 1.67 | D.6 | 4.64 | 769.95 | 0.58 |
| D.3 | 10.667 | 1770 | 1.33 | D.7 | 3.2 | 531 | 0.40 |
| D.4 | 8 | 1327.5 | 1.00 | | | | |
| E.1 | 15 | 265.5 | 2.00 | E.4 | 7.5 | 132.8 | 1.00 |
| E.2 | 12.5 | 221.3 | 1.67 | E.5 | 5.7 | 100.9 | 0.76 |
| E.3 | 9.487 | 167.9 | 1.26 | | | | |
| F.1 | 14.222 | 2655 | 2.00 | F.5 | 5.4044 | 1008.9 | 0.76 |
| F.2 | 11.852 | 2212.5 | 1.67 | F.6 | 4.1244 | 769.95 | 0.58 |
| F.3 | 9.4815 | 1770 | 1.33 | F.7 | 2.8444 | 531 | 0.40 |
| F.4 | 7.1111 | 1327.5 | 1.00 | | | | |
| G.1 | 15 | 2655 | 2.00 | G.4 | 7.5 | 1327.5 | 1.00 |
| G.2 | 12.5 | 2212.5 | 1.67 | G.5 | 5.7 | 1008.9 | 0.76 |
| G.3 | 10 | 1770 | 1.33 | G.6 | 4.5 | 796.5 | 0.6 |

TABLE 2. Case A. Free-stream fast acoustic waves: $Re_\infty = 6026.6$, $T_w^* = 1000\,\text{K}$, $r^* = 0.0125\,\text{m}$, $d^* = 0.1\,\text{m}$. $T_\infty^* = 192.989\,\text{K}$, $p_\infty^* = 10.3\,\text{Pa}$, $\gamma = 1.4$, $Pr = 0.72$. $M_\infty = 15$, $\epsilon = 5 \times 10^{-4}$ to $10^{-1}$. Parameters in Sutherland's viscosity formula: $T_r^* = 288\,\text{K}$, $T_s^* = 110.33\,\text{K}$, $\mu^* = 0.17894 \times 10^{-4}\,\text{kg}\,\text{m}^{-1}\,\text{s}^{-1}$. Case B. Free-stream entropy waves: all conditions same as case A. Case C. Free-stream slow acoustic waves: all conditions same as case A. Case D. Free-stream vorticity waves: all conditions same as case A. Case E. Reynolds number effects: all conditions same as case A except $r^*$, $d^*$, $Re_\infty$ are 10 times larger; $Re_\infty = 60\,266$. Case F. Mach number effects: $M_\infty = 8$ while other non-dimensional parameters are the same as case A. Case G. Wall temperature effects: $T_w^* = 2000\,\text{K}$ and $T_w/T_0 = 0.2253$, while other non-dimensional parameters are the same as case A.

effects on steady flow solutions of pressure profiles behind the bow shock and on the body surface. The results from the two sets of grids are indistinguishable. The numerical errors can be quantitatively evaluated using the Richardson extrapolation method. The $L_1$ relative error for pressure ($\|\Delta p/p\|_1$) on the body surface is $1.7 \times 10^{-6}$ for the current test case, and that for the bow shock location is $5.0 \times 10^{-7}$. For steady solutions, the simulation is treated as an unsteady flow with shock motions. The solution is advanced in time without free-stream disturbances. A steady state is reached in the flow field when local velocities of the bow shock converge to zero. Therefore, it is necessary to ensure the steady solution is a converged solution with zero shock velocity. In the steady solution presented in this paper, the maximum relative velocity of the bow shock is $2.8 \times 10^{-12}$.

A grid refinement is also used to check the numerical resolution of the $160 \times 120$ grid for unsteady receptivity simulations. As an example of such a grid refinement
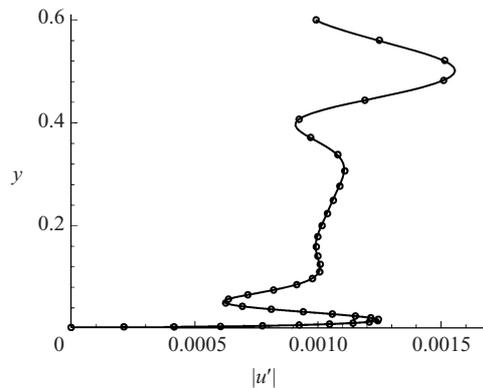
FIGURE 46. Unsteady flow solutions for case A.1 for $F = 2655$ for variation of $|u'|$ along a grid line normal to the parabola surface at $x = 0.239$ (line: $320 \times 240$ grid, and circles: $160 \times 120$ grid).

study, the variation of the Fourier perturbation amplitudes of velocity $|u'|$ along a grid line normal to the parabola surface at $x = 0.239$ is shown in figure 46. The unsteady solutions obtained by using two sets of grids, $320 \times 240$ and $160 \times 120$ grids, agree very well with each other. This figure shows that the unsteady solutions presented in this paper are adequately resolved by the $160 \times 120$ grid for the first computational zone used in most of the calculations for the results presented in this paper.

REFERENCES

BUTER, T. A. & REED, H. L. 1994 Boundary layer receptivity to free-stream vorticity. *Phys. Fluids* **6**, 3368–3379.

CASALIS, G. & CANTALOUBE, B. 1994 Receptivity by direct numerical simulation. In *Direct and Large-Eddy Simulation I* (ed. P. R. Voke *et al.*), pp. 237–248. Kluwer.

CHOUDHARI, M. & STREETT, C. L. 1993 Interaction of a high-speed boundary layer with unsteady free-stream disturbances. In *Transitional and Turbulent Compressible Flows* (ed. L. D. Kral & T. A. Zang). FED-Vol. 151, pp. 15–28. ASME.

COLLIS, S. S. & LELE, S. K. 1996 A computational approach to swept leading-edge receptivity. *AIAA Paper* 96-0180.

GOLDSTEIN, M. E. 1983 The evolution of Tollmien-Schlichting waves near a leading edge. *J. Fluid Mech.* **127**, 59–81.

HADDAD, O. M. & CORKE, T. C. 1998 Boundary layer receptivity to free-stream sound on parabolic bodies. *J. Fluid Mech.* **368**, 1–26.

HERBERT, T. & ESFAHANIAN, V. 1993 Stability of hypersonic flow over a blunt body. In *AGARD CP* 514, pp. 28.1–28.12.

HORNUNG, H. G. 1998 Gradients at a curved shock in reacting flow. *Shock Waves* **8**, 11–21.

HU, S. H. & ZHONG, X. 1998 Linear stability of viscous supersonic plane Couette flow. *Phys. Fluids* **10**, 709–729.

KENDALL, J. M. 1975 Wind tunnel experiments relating to supersonic and hypersonic boundary-layer transition. *AIAA J.* **13**, 290–299.

KOVASZNAY, L. S. G. 1953 Turbulence in supersonic flow. *J. Aero. Sci.* **20**, 657–682.

KUFNER, E., DALLMANN, U. & STILLA, J. 1993 Instability of hypersonic flow past blunt cones – effects of mean flow variations. *AIAA Paper* 93-2983.

LEES, L. & LIN, C. C. 1946 Investigation of the stability of the laminar boundary layer in compressible fluid. *NACA TN* 1115.

MACK, L. M. 1984 Boundary layer linear stability theory. *AGARD Rep.*, pp. 3–1 to 3–81.

MALIK, M. R., SPALL, R. E. & CHANG, C.-L. 1990 Effect of nose bluntness on boundary layer stability and transition. *AIAA Paper* 90-0112.

MCKENZIE, J. F. & WESTPHAL, K. O. 1963 Interaction of linear waves with oblique shock waves. *Phys. Fluids* **11**, 2350–2362.

MORKOVIN, M. 1969 On the many faces of transition. In *Viscous Drag Reduction* (ed. C. Wells), pp. 1–31. Plenum.

MURDOCK, J. W. 1981 Tollmien-Schlichting waves generated by unsteady flow over parabolic cylinders. *AIAA Paper* 81-0199.

POTTER, J. L. & WHITFIELD, J. D. 1962 Effects of slight nose bluntness and roughness on boundary-layer transition in supersonic flows. *J. Fluid Mech.* **12**, 501–535.

RESHOTKO, E. & KHAN, N. M. S. 1980 Stability of the laminar boundary layer on a blunt plate in supersonic flow. In *IUTAM Symp. on Laminar-Turbulent Transition* (ed. R. Eppler & H. Fasel), pp. 186–190. Springer.

RESHOTKO, E. 1991 Hypersonic stability and transition. In *Hypersonic Flows for Reentry Problems, Vol. 1* (ed. J.-A. Desideri, R. Glowinski & J. Periaux), pp. 18–34. Springer.

STETSON, K. F., THOMPSON, E. R., DONALDSON, J. C. & SILER, L. G. 1984 Laminar boundary layer stability experiments on a cone at Mach 8, part 2: blunt cone. *AIAA Paper* 94-006.

STETSON, K. F. & KIMMEL, R. L. 1992 On hypersonic boundary layer stability. *AIAA Paper* 92-0737.

TRUESDELL, C. 1952 On the curved shocks in steady plane flow of an ideal fluid. *J. Aero. Sci.* **19**, 826–828.

ZHONG, X. 1996 Additive semi-implicit Runge-Kutta schemes for computing high-speed nonequilibrium reactive flows. *J. Comput. Phys.* **128**, 19–31.

ZHONG, X. 1998 High-order finite-difference schemes for numerical simulation of hypersonic boundary-layer transition. *J. Comput. Phys.* **144**, 662–709.